

Review of superconducting transition-edge sensors for x-ray and gamma-ray spectroscopy

This content has been downloaded from IOPscience. Please scroll down to see the full text.

2015 Supercond. Sci. Technol. 28 084003

(<http://iopscience.iop.org/0953-2048/28/8/084003>)

View [the table of contents for this issue](#), or go to the [journal homepage](#) for more

Download details:

IP Address: 132.163.136.19

This content was downloaded on 27/10/2015 at 16:22

Please note that [terms and conditions apply](#).

Review of superconducting transition-edge sensors for x-ray and gamma-ray spectroscopy*

Joel N Ullom^{1,2} and Douglas A Bennett^{1,3}

¹National Institute of Standards and Technology, Boulder, CO, USA

²University of Colorado, Boulder, CO, USA

E-mail: Joel.Ullom@nist.gov and Douglas.Bennett@nist.gov

Received 19 March 2015, revised 21 May 2015

Accepted for publication 29 May 2015

Published 13 July 2015



Abstract

We present a review of emerging x-ray and gamma-ray spectrometers based on arrays of superconducting transition-edge sensors (TESs). Special attention will be given to recent progress in TES applications and in understanding TES physics.

Keywords: superconducting detector, microcalorimeters, x-ray spectroscopy

(Some figures may appear in colour only in the online journal)

1. Introduction

One role where superconducting electronics have found considerable recent success is as detectors of photons and particles. However, the field of low temperature detectors, which includes superconducting sensors, was last reviewed in 2005 [1]. Since that time, two developments have occurred which motivated the preparation of this article. The years since 2005 have seen the emergence and early applications of complete x-ray and gamma-ray spectrometers based on arrays of superconducting transition-edge sensors (TESs). TESs are thermal detectors that rely on the steep resistive transition of a superconducting material as a thermometer. Arrays of TESs already provide collecting areas and count rates that are two orders of magnitude larger than results from single devices. These improvements have begun to make practical a range of applications in laboratory and large facility settings. The second motivating development is the very considerable recent progress towards understanding the underlying physics of TES devices. In addition to answering fundamental questions such as the origins of resistance in TESs, this work has implications for the optimal design and operation of TES devices. Here, we present a review of TES detectors for x-ray and gamma-ray spectroscopy as well as developments in the

understanding of these devices. The remarkable progress made recently in the development and use of superconducting detectors including TESs for other applications such as millimeter-wave astrophysics falls outside the scope of this article.

The underlying motivation for the use of low temperature detectors is the suppression of thermal noise and the ready accessibility of quantum-mechanical phenomena at cryogenic temperatures. Superconductivity is a quantum phenomenon that appears at low temperatures and that plays several important roles in the emergence of low temperature detectors. Superconducting materials are used in sensing elements, sometimes in the supporting cryogenics, and often in the cryogenic read-out circuits that enable sensor arrays. Read-out techniques for superconducting detectors are also reviewed in this article.

The suppression of thermal noise at low temperatures enables energy or power deposited by photons and particles to be measured with great precision. In the case of x-rays and gamma-rays, the energy of single photons can be measured with resolving powers $E/\Delta E > 10^3$. This quality of spectroscopy is significantly better than can be accomplished with scintillating or even semiconducting sensors such as high-purity germanium (HPGe) and silicon drift detectors (SDDs). In fact, these resolving powers are competitive with the results of wavelength dispersive measurements using crystals or gratings. However, arrays of superconducting detectors

* Contribution of a U.S. government agency, not subject to copyright.

³ Author to whom any correspondence should be addressed.

retain the key attractions of simpler energy dispersive tools. These attractions include large collecting areas, high absorption efficiency, a compact footprint, wide energy acceptance, and a simple efficiency curve. Hence, superconducting x-ray and gamma-ray detectors combine the superior resolving power of wavelength dispersive techniques with the large collection capability and simplicity of operation of energy dispersive techniques. This combination of desirable qualities was not a foregone conclusion and instead is the result of considerable recent technological progress. We will also describe several contemporary instruments based on superconducting detectors.

2. Components of superconducting x-ray and gamma-ray detectors

A single detector must perform several functions, functions that are sometimes performed by distinct structures within the sensor. One structure in a detector must absorb incident photons and convert the energy of the photon into heat or other measurable excitations. Another structure must transduce heat or other excitations into a measurable electrical signal. A detector must also be partially isolated from the outside world; if the energy of an incident photon is not temporarily confined in a finite body, it cannot be precisely measured. Sometimes the isolation of a detector is accomplished by a carefully designed component and sometimes it is accomplished using the thermal impedances that arise naturally at low temperatures. In this section, we describe sensing, absorbing, and isolating structures for TESs.

2.1. Sensing structures

Sensing structures divide naturally into thermal and athermal detection mechanisms. Thermal sensors, which include TESs, detect a temperature change. It can be shown that the RMS energy fluctuations in a thermally isolated heat capacity C at temperature T due to the exchange of energy with a thermal bath also at T are given by $(k_b T^2 C)^{1/2}$ [2]. This quantity, sometimes referred to as the thermodynamic limit, is not the precision limit of a calorimetric energy measurement. Other factors play a role including the quality of the thermometer as well as the sources of broad-band noise in the measurement. However, the resulting detailed expressions invariably are proportional to the simple equation above. Hence, measurement precision is improved when C and T are small. The most common type of thermal superconducting sensor is the TES in which the resistance of a film biased in the superconducting-to-normal transition changes in response to a temperature excursion caused by deposited energy. A detailed expression for the energy resolution of a TES detector in the small signal limit can be found in [1]. In the small signal limit, the resistance excursion due to an absorbed photon is small compared to the quiescent TES resistance. The best TES energy resolutions achieved to date are 1.6 eV FWHM at 5.9 keV [3] and 0.9 eV FWHM at 1.58 keV [4]. An example Mn-

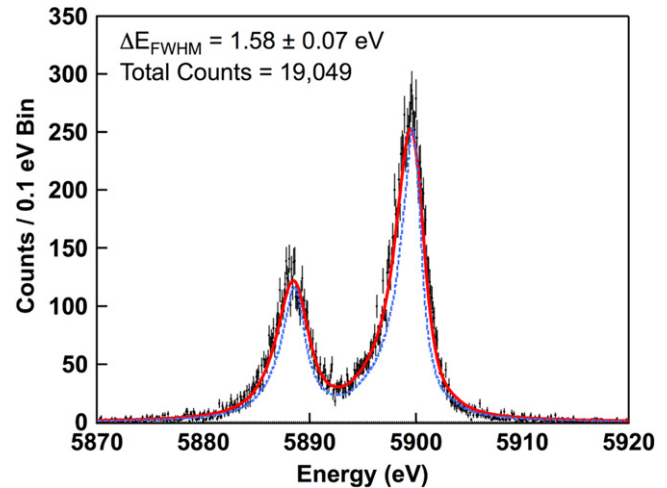


Figure 1. TES spectrum of the Mn-K α x-ray complex near 5895 eV demonstrating excellent resolution. The dashed blue line is the natural lineshape of the complex. Figure courtesy of Steve Smith, NASA Goddard Space Flight Center.

K α spectrum demonstrating this excellent resolution is shown in figure 1.

A wide variety of films have been successfully used as TESs. For high resolution spectroscopy, the transition temperature is usually chosen to be as low as can be achieved using readily available cryogenics, or around 50–100 mK. However, higher transition temperatures can be tolerated in some cases such as when resolution is limited by factors other than thermodynamic fluctuations. Films with desirable transition temperatures have been achieved using elemental superconductors (such as W), alloys (such as Al-Mn), and proximity-coupled bilayers or multilayers (such as Mo-Cu, Mo-Au, and Ti-Au). The TES film is contacted by superconducting leads with a higher T_c and I_c . A crucial innovation is the use of voltage-biased readout achieved by placing the TES in parallel with a smaller shunting resistor [5]. The current through the TES, which depends on its resistance and temperature, is measured by a SQUID ammeter placed in series with the sensor. A detailed discussion of resistance mechanisms in TESs is given in section 5.2.

In the small signal limit, the behavior of TESs can be described using the solutions to a pair of coupled differential equations representing the electrical and thermal circuits [5–8]. These references also describe the fundamental sources of TES noise in the small signal limit. The complexity of the resistive transition is captured by two logarithmic derivatives: $\alpha = (T/R)(dR/dT)$ and $\beta = (I/R)(dR/dI)$ that can be measured at a particular bias point even if they cannot be predicted theoretically. These results are well summarized in previous work and will not be repeated here. However, TES x-ray and gamma-ray detectors are routinely operated outside the small signal limit because dynamic range is in tension with energy resolution [9]. To describe TES behavior in the large signal limit, it is necessary to understand the true shape of the resistance surface $R(I, T)$ where resistance varies with current and temperature. The transition shape also depends on the local magnetic field B which can be caused by external

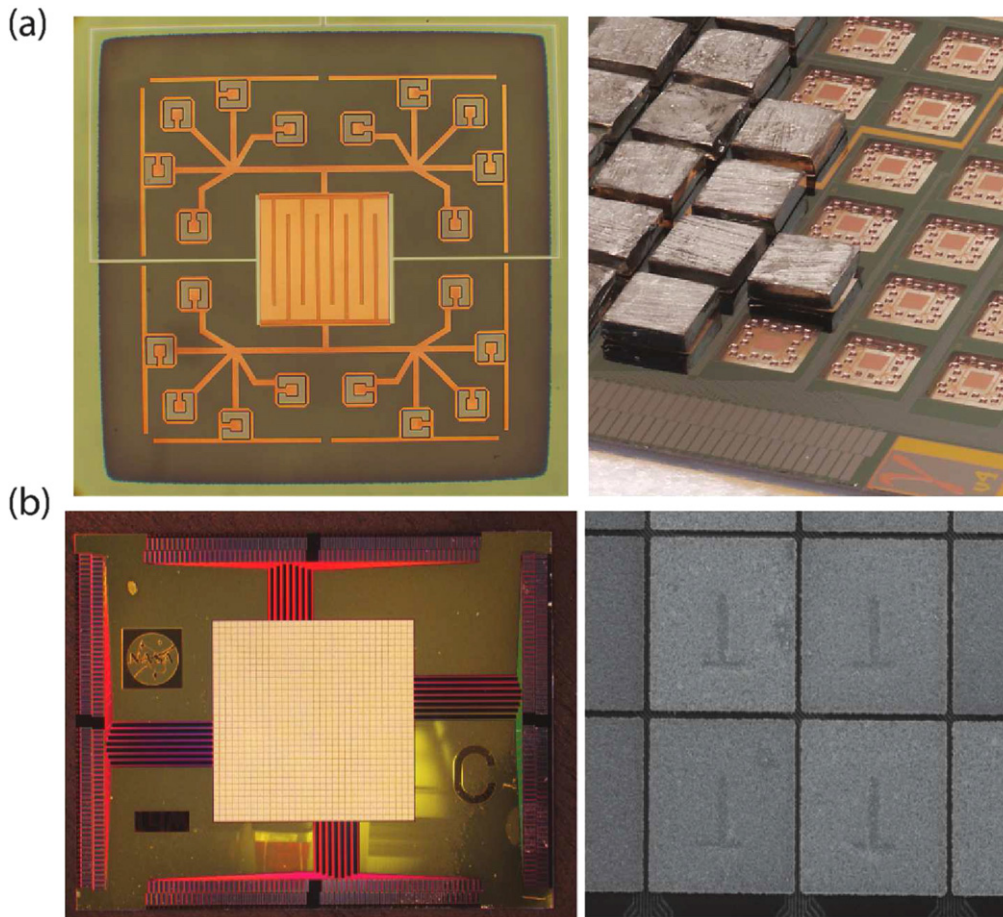


Figure 2. (a) On the left, micrograph of a TES for gamma-ray spectroscopy. Superconducting molybdenum leads contact the left and right sides of a molybdenum-copper bilayer TES at the center. Interdigitated normal films are added to the TES. A network of normal films connects the TES to horse-shoe shaped epoxy posts. A bulk absorber is later attached to the top of the posts. Energy leaving the absorber is conducted to the TES through the normal layer. All these thin-film components are located on top of a relieved SiN membrane that appears dark green in the photo. On the right, micrograph of an array of such TESs. Bulk superconducting tin absorbers have been attached to some sensors in the array. Reprinted with permission from [40]. Copyright 2012, AIP Publishing LLC. (b) On the left, micrograph of an 32×32 array of x-ray TES sensors with overhanging absorbers. On the right, a zoomed view of a few of the TESs from this array. The sensing bilayer is hidden by an elevated $242 \times 242 \mu\text{m}$ thin-film bismuth absorber. The absorber contacts the TES in the T-shaped region only. The details of these overhanging absorbers is described in Iyomoto *et al* [41]. Photographs courtesy of Caroline Kilbourne, NASA Goddard Space Flight Center.

sources or the bias current of the TES itself; hence, it is reasonable to consider the still more complicated $R(I, T, B)$ surface. The resistance surface depends on the underlying physics of the resistive transition and, in particular, on the resistance mechanism. Significant progress has been made in the last decade understanding the resistance mechanism of TESs and this work is reviewed in section 5. With expressions for $R(I, T)$, it becomes possible to evaluate TES performance under more realistic conditions where absorbed photons produce large temperature and resistance excursions.

A photograph of a TES sensor is shown in figure 2(a). The interdigitated structures on top of the TES are additional normal metal films whose presence regulates current flow and helps to control the transition width and device noise [10, 11]. Prior to the introduction of normal metal structures, broadband noise whose amplitude exceeded the expected nonlinear Johnson noise was commonly observed in TESs. With these structures, noise levels near the nonlinear Johnson limit are

routinely but not always achieved. The physical origin of the so-called excess or unexplained noise remains unclear but its dependencies have been heavily studied [12, 13].

Other thermal sensing structures include heavily-doped semiconductors whose resistance continues to depend on temperature in the cryogenic regime and thin films with temperature-dependent magnetic properties. While not the focus of this article, these devices deserve brief mention. Semiconducting detectors have achieved good resolution levels for x-ray and gamma-ray spectroscopy [14, 15] but lower values of the logarithmic derivative of resistance with temperature typically produce inferior resolution and speed compared to TESs. Further, the absence of a multiplexing scheme has limited x-ray and gamma-ray arrays to tens of devices. Magnetic sensors have achieved resolution values comparable to TESs and may achieve better resolution in the future [16]. However, multiplexing these devices is more

challenging than TESs and work towards sensor arrays is still at a very early level of development.

Athermal sensors measure excitations, typically superconducting quasiparticles, created by an incident particle or photon. Examples include superconducting tunnel junctions (STJs) and microwave kinetic inductance detectors (MKIDs). To date, the resolution of STJs and MKIDs is inferior to TESs [17–19] and the absence of a multiplexing scheme for STJs is an obstacle to their use in large arrays. In contrast, high multiplexing factors are possible with MKIDs. In recent work, MKIDs have been used as thermal sensors for the temperature of an isolated platform in much the same way as TESs [20].

2.2. Absorbing structures

TES detectors typically rely on photoelectric absorption of x-rays and gamma-rays. The absorbed photon is annihilated and its energy E_g is transferred to a single electron that acquires kinetic energy $E_g - E_b$ where E_b is its previous binding energy. The hot photoelectron then relaxes to the Fermi level by electron-electron and electron-phonon scattering. The energy lost in a single electron-phonon event is limited to $k_b T_D$ where T_D is the Debye temperature or 10's of meV so electron-electron scattering is initially a more efficient cooling mechanism. As electronic excitations approach the Fermi level, cooling by electron-phonon scattering becomes more important. Hot phonons either excite additional electrons or escape to the heat bath. The escape of hot phonons corresponds to lost signal and event-to-event fluctuations in this loss are a source of noise [21, 22].

Superconducting detectors are often designed to reduce these losses either by locating the absorber on a micro-machined membrane or by isolating the absorber above the substrate on small-area supports as shown in figure 2. The initial relaxation cascade is completed within about 10^{-10} seconds depending on the material, and results in a partitioning of the energy of the absorbed photon among the electron and phonon systems of the absorber. In a normal metal, electronic energy takes the form of an increased electron temperature; in a superconductor, electronic energy takes the form of additional quasiparticles. Several authors have treated the rapid relaxation cascade and estimated the subsequent division of energy among electrons and phonons [23–25].

In an ideal absorber, all the energy of the photon is converted to a measurable form resulting in a well-defined photopeak whose width is limited by noise mechanisms after the initial thermalization process. However, numerous non-idealities are possible. Even at very low levels, Compton scattering produces a weak continuum of events below the main photopeak as scattered photons can leave the sensor resulting in partial energy deposition. The likelihood of Compton scattering grows with photon energy for the energies likely to be encountered by TES detectors [26]. The escape of some of the initial hot photoelectrons from an exterior surface of the absorber will also produce a weak low-energy continuum [27, 28]. The amplitude of this continuum

is operationally important since it affects the ease of observing weak photopeaks at energies below a stronger spectral feature [29]. The composition of the absorber can also contribute non-idealities. Insulating absorbers work poorly because of the creation of long-lived electronic excitations during the relaxation cascade that are lost to the subsequent energy measurement. Since the energy to create an electron-hole pair is about 10 eV in an insulator, even small event-to-event fluctuations in the number of such pairs will degrade sensor resolution. Similar effects can occur in semiconductors with finite gaps. Normal metals, semimetals, zero-gap semiconductors, and some superconductors have worked well as absorbers because they quickly and reproducibly thermalize close to 100% of deposited energy.

In superconducting detectors for photons below about 1 keV of energy, the sensing structure usually provides enough stopping power to also act as the absorber. For higher energy photons, an absorber is usually needed. For thermal detectors such as TESs, the absorber should combine high stopping power, low heat capacity, and good thermalization properties. Between 1 and 10 keV, the absorber is typically another film in good thermal contact with the sensing element. The semimetal bismuth is widely used because of its high atomic number ($Z = 83$) and very low specific heat. Gold is also commonly used because of its high atomic number ($Z = 79$) and low specific heat for a normal metal. An absorber containing 3 μm of gold has a 92% chance of absorbing a 6 keV photon.

At energies above 10 keV, absorption in thin films becomes less likely. Electrodeposition can be used to grow films 10's or 100's of microns thick to absorb high energy photons. Alternatively, a bulk foil prepared separately can be attached to a thin-film sensor. This attachment is most easily done with a cryogenic epoxy, but use of an insulating epoxy implies that energy can only leave the foil in the form of phonons. Superconducting absorbers are attractive because the electronic contribution to the specific heat of a superconductor scales as $e^{-T_c/T}$. For $T/T_c \approx 0.1$, this contribution is effectively zero which preserves energy resolution. However, achieving rapid and efficient thermalization of energy deposited in bulk superconductors remains a challenge and the use of bulk superconducting absorbers is an active area of research [25]. In this context, we take thermalization to mean the conversion of photon energy into phonon energy that can leave the absorber and heat the sensor. Simple models of energy thermalization in a bulk superconductor predict that energy will remain in the quasiparticle system for impractical lengths of time because the time for a recombination phonon produced by the annihilation of two quasiparticles to break another Cooper pair is typically much shorter than the time for a recombination phonon to exit bulk material through a glue joint. This effect results in a greatly extended quasiparticle lifetime. However, actual pulse durations from some superconductors (Pb, In, and Sn for example) are far shorter than the calculated thermalization times, posing the question of why these superconductors work as absorbers as well as they do. Thermalization in superconducting tin ($Z = 50$) is

particularly fast and complete. Trapped flux, impurities, and other sources of local energy-gap suppression may accelerate quasiparticle recombination and lead to the generation of recombination phonons that cannot break Cooper pairs in the higher gap regions of pristine material, thus facilitating phonon escape. Further, recent work indicates that the intrinsically anisotropic energy gap and density of states in clean, bulk tin powerfully accelerate thermalization [30].

Bulk absorbers are often attached to a sensing structure by a cryogenic epoxy [31–34]. However, it has recently been shown that at least some epoxies are the source of extended heat release after the absorption of a photon that delays sensor recovery and is easily mistaken for slow thermalization in the absorber. When a metallic joint was used to connect a Sn absorber to a TES thermometer, >95% of deposited energy emerged from the device on prompt timescales indicating that thermalization occurred much faster than the thermal time constants of the device [35].

Certain superconducting materials such as tantalum are, in principle, extremely attractive for x-ray and gamma-ray absorbers. Tantalum has a high atomic number ($Z = 73$) and a high Debye temperature so that its phononic specific heat is very low. However, detectors using bulk tantalum absorbers show time constants of 10^{-2} s or longer that are largely impractical [36]. While these extended time constants may be due to slow thermalization, both historical and contemporary measurements of the heat capacity of Ta are much higher than the expected phononic contribution, an excess which will slow device recovery [37, 38]. In contrast, both historical and contemporary measurements of the heat capacity of Sn are close to the expected values [38, 39].

While rare, other absorbing schemes combine athermal and thermal processes. For example, phonons or quasiparticles created in a large volume absorber can be coupled to a smaller sensor. Some resolution degradation is often associated with such schemes.

2.3. Thermal isolation

If a thermal detector is in near perfect thermal contact with the outside world, then the pulses created by incident x-rays and gamma-rays will be so fast that they exceed the bandwidth of realistic amplifiers. Hence, some thermal isolation is necessary. A thermal impedance to the outside world that significantly exceeds the thermal impedances within a device also helps ensure that the device response is independent of the position where a photon is absorbed.

Thermal isolation can be achieved via electron-phonon decoupling, acoustic mismatch at film interfaces, or by limiting phonon transport. Phonon transport can readily be tailored using geometry and material choice. TES detectors have been isolated on patterned SiN and SOI membranes with thicknesses of about 100 nm to a few microns. Detectors have also been isolated using full-thickness Si wafers patterned into meandering beams. Detectors can be fabricated on bulk substrates using a combination of electron-phonon decoupling and acoustic mismatch for thermal isolation. The power flow due to acoustic mismatch scales as film area and the fourth

power of temperature. Power flow due to electron-phonon decoupling scales as film volume and usually as the fifth or sixth power of temperature. So, electron-phonon decoupling will be the limiting thermal impedance at very low temperatures and in very thin films. As mentioned above, the escape of phonons created during the initial relaxation cascade is a risk in devices on bulk substrates that can be avoided by elevating the absorber as shown in figure 2. We conclude by noting that electronic energy is prevented from leaving the TES through the higher gap leads because of the low electronic thermal conductivity of superconductors and because of Andreev reflection at the TES-lead interface.

3. Sensor readout

The choice of readout approach for cryogenic sensors is highly dependent on the type of sensor being measured. In some cases there is a natural choice for the readout. For example, MKIDs are constructed from microwave resonators and so are naturally measured in the frequency domain. TESs are almost always measured using SQUIDs as sensitive ammeters. SQUIDs are compatible with a number of different readout implementations. The independence of the measurement SQUIDs from the TES sensors poses some mechanical complexities but also allows separate optimization of the sensors and readout. Crucially, SQUIDs enable multiplexed readout of TESs meaning the readout of many sensors using a smaller number of amplifier channels. Multiplexing has proven crucial to the development of large arrays of sensors since it reduces the mechanical, thermal, and financial burden of having readout circuitry for each pixel. Some other cryogenic sensors, i.e. silicon thermistors and STJs, lack a readout that is compatible with multiplexing. The most noticeable difference between multiplexing implementations is the choice of the basis that is used to separate the signals from different sensors [8, 42]. The different modulation functions being pursued for TESs are shown in figure 3. Besides the encoding and decoding steps, multiplexing also requires the combination of different sensor signals into a smaller number of channels. This combination necessitates a band-pass limiting filter for each sensor so that their broad-band noise contributions are not summed.

Multiplexing is almost always important in x-ray and gamma-ray applications where large arrays of cryogenic sensors are needed to boost collection efficiency and count rate. For x-ray and gamma-ray applications, much of the progress since the last major review of cryogenics sensors [1] has been enabled by the emergence of array-scale readout systems. In what follows, we provide brief summaries of the different types of SQUID multiplexing, review progress achieved in the last decade, and describe the advantages and disadvantages of each approach. The discussion is organized by multiplexing basis set. Proceeding in order of technical maturity, we will discuss time-division multiplexing (TDM), code-division multiplexing (CDM), and low-frequency frequency-division multiplexing (FDM), followed by promising recent results from microwave resonator based readout.

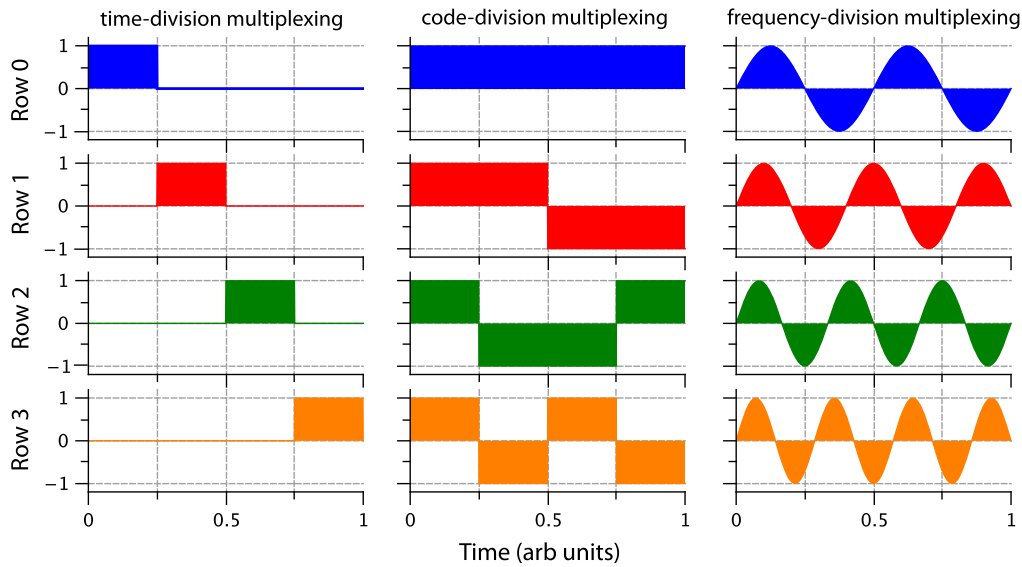


Figure 3. Orthogonal modulation functions for four channels in each of the basis sets for multiplexing TES microcalorimeters. The output gain for each basis is plotted as a function of time in arbitrary units.

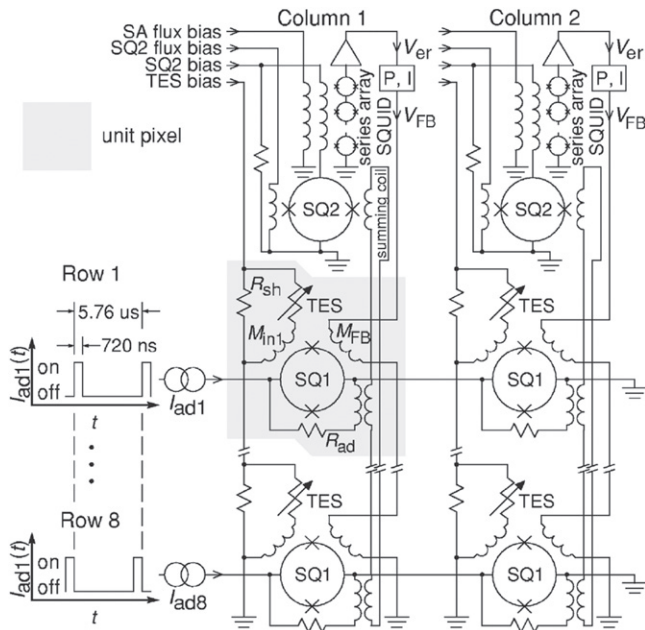


Figure 4. A schematic representation of a 2 column by 8 row TDM circuit. Each row is turned on sequentially, with the control bias to turn on the SQUIDs corresponding to a given row in all the columns connected in series. Reproduced from Doriese *et al.* Reprinted with permission from [40]. Copyright 2007, AIP Publishing LLC.

3.1. Time-division multiplexing

TDM consists of combining the signals from a series of sensors into a single shared amplifier chain by separating them in the time domain [43]. Each sensor in TDM has a dedicated first stage SQUID. The measurement sequence for a column of sensors consists of turning on one of the SQUIDs, waiting for transients to settle, averaging over some measurement period, and then repeating for the next SQUID in the column. As shown in figure 4, a TDM multiplexer is

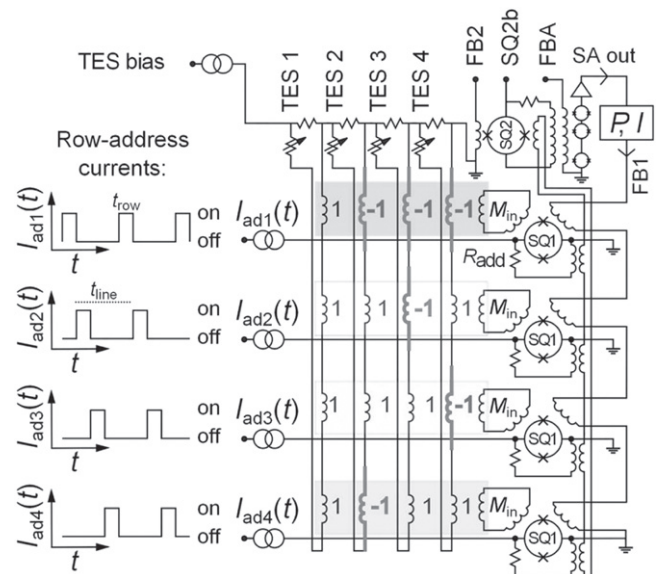


Figure 5. A schematic representation of four-row Φ -CDM. The current signal from a given TES is inductively coupled to all four first-stage SQUID amplifiers with coupling polarity defined by the appropriate column of the Walsh basis set. The rows are activated sequential as in TDM. The signals from all the SQUID1's (SQ1) are summed into SQUID2 (SQ2) which is coupled to a SQUID series amplifier (SA). The dynamic range is extended by implementing a flux-lock loop using feedback applied to the SQ1s as in TDM. Reprinted with permission from [56]. Copyright 2012, AIP Publishing LLC.

designed so that a single pair of control lines can turn on SQUIDs in otherwise distinct columns. An M column by N row TDM SQUID multiplexed readout needs on the order of $M + N$ signal lines instead of $M \times N$ that would be necessary if each detector had its own readout chain.

The bandwidth of each measurement is set by the boxcar modulation function, see figure 3, such that the noise bandwidth is $1/2\delta t_s$, where δt_s is the time the multiplexer dwells on

a given pixel. The rate at which all the pixels in a column are measured, the so-called frame rate, depends on the number of pixels in a column (N) as $1/(N\delta t_s)$. Noise above the Nyquist frequency of the frame rate, $1/(2N\delta t_s)$, but below the measurement bandwidth is aliased into the signal band. Typically, only SQUID noise is present at these frequencies because of the L/R roll-off of the TES bias circuit. Therefore, the effective SQUID current noise scales as \sqrt{N} . For a fixed current response from a TES, increasing the mutual inductance between sensors and SQUIDs reduces the effective current noise at the expense of increased signal slew rates. To maintain a flux-locked loop at each SQUID [45], feedback signals are computed after each SQUID measurement, stored, and applied the next time that sensor is measured. If the signal slew rates are too large, flux-lock can be lost and the signal from that sensor is corrupted. The correct choice of the inductance in series with the TES can moderate the slew rate on the rising edge of pulses and shorten pulse durations, even for complex two-body sensors [46].

At the moment, TDM is the most mature of the TES multiplexing architectures and has achieved the largest arrays both for TES microcalorimeters and bolometers [47]. To date, the shortest time demonstrated for turning on and measuring a SQUID is 320 ns. Work is underway to reduce this interval to 160 ns. TDM has been used to demonstrate 3.0 eV FWHM resolution at 5.9 keV in a 2 column by 16 row array of x-ray TESs [48]. TDM has been used to measure 256 TESs in 8 columns of 32 rows in an instrument optimized for 200 keV gamma-rays [40]. Recently, TDM has also been demonstrated with magnetically coupled calorimeters [49].

Because spectrometers that use TDM have been in operation for several years now, there has been an opportunity for some engineering refinements. Unlock events in the SQUIDs can be detected and rapidly restored in the firmware of the digital feedback electronics. Further, there is a growing understanding of sources of cross-talk. Besides operational improvements, TDM circuit architectures continue to evolve and improve. A number of groups have pursued current steered switches which, among other benefits, make TDM circuitry more robust to variation in the critical current in the SQUID fabrication process [50–52].

The major advantages of TDM are its simplicity and maturity. A useful feature of TDM is that it is straightforward to turn off the multiplexing and measure a single TES. Since the TES bias is not modulated, this is the simplest possible operational state. The ability to fall back to non-multiplexed, DC-biased readout can be helpful in debugging an instrument or performing single pixel characterization. The chief disadvantage of TDM is the \sqrt{N} noise penalty. The chief optimization in TDM is the balance between SQUID noise and maintaining flux lock on the leading edges of pulses.

3.2. Code division multiplexing

Code-division multiplexing combines many of good features of TDM with the potential to read out larger arrays or faster pixels [53, 54]. The orthogonal modulation functions for CDM are the Walsh codes [55]. An example of a Walsh code

for four channels is shown in figure 3. It can be seen that, at any instant, the signals from all the sensors are combined with different polarities. The combination of polarities changes between measurements. Then, a matrix inversion is performed on a sequence of measurements to separate the signals from the individual sensors. Since the signals are switched like in TDM, CDM requires bandwidth higher than the Nyquist bandwidth. Therefore the SQUID noise is degraded by \sqrt{N} due to aliasing. However, since all the pixels are measured all the time, N independent samples of each input signal are obtained, boosting the signal-to-noise ratio by \sqrt{N} . The factors of \sqrt{N} cancel so there is no noise penalty for adding more sensors. Since CDM does not suffer a \sqrt{N} noise penalty, the coupling to the SQUIDs can be smaller than in TDM. A smaller coupling increases the dynamic range of the SQUID, which enables the readout of more or faster pixels. The sensors remain DC biased as in TDM.

Currently there are two implementations of CDM which use different mechanisms to switch the polarity of the sensor signals [53]: flux summation (Φ -CDM) and current steering (I-CDM). Neither of these mechanisms modulates the polarity of the TES bias, as was proposed in early CDM multiplexing schemes [57]. Φ -CDM uses N input coils coupled to all N SQUIDs in different polarity configurations to code the Walsh modulation. A four-row example of Φ -CDM is described in figure 5. The signals from the N SQUIDs are measured sequentially as in TDM. The major drawback to Φ -CDM is that every TES is connected to every SQUID. The signal routing length and therefore the lithographic fabrication complexity increase as N^2 . The major advantage is that it is straight forward to move from existing TDM systems to Φ -CDM.

I-CDM uses a superconducting switch to modulate the polarity of the signals coupled to the SQUIDs. All the TESs couple to the same SQUID with different patterns of polarities modulated by superconducting switches. The switched nature of I-CDM allows the TESs to be dc voltage biased without the need of a shunt resistor. The bias is inductively coupled into the readout loop passing through the polarity switches in such a way that the TESs which are on the other side of the low pass filter see an essentially constant dc bias [54]. By controlling the ramp signal that is coupled to the loop, each TES can be set to its optimum bias without the dissipation that occurs when using a shunt resistor. The lower power dissipation per TES could be important for larger arrays of TESs. The reduced dissipation in the TES and ability to avoid the \sqrt{N} noise penalty make I-CDM a promising technology for mega-pixel arrays of TES microcalorimeters. One implementation of the switch is to have low inductance dc SQUIDs in the two arms of the switch biased π out of phase from each other such that a flux input determines which arm of the switch conducts current [50].

Φ -CDM and I-CDM have both been demonstrated at small pixel counts. In 2010 Niemack *et al* [51] demonstrated a four row I-CDM circuit with no \sqrt{N} dependent noise penalty and low levels of crosstalk. An eight row Φ -CDM measurement was performed in 2012 by Stiehl *et al* [56]. The effective SQUID noise was 19 pA/Hz^{1/2} and the x-ray TESs

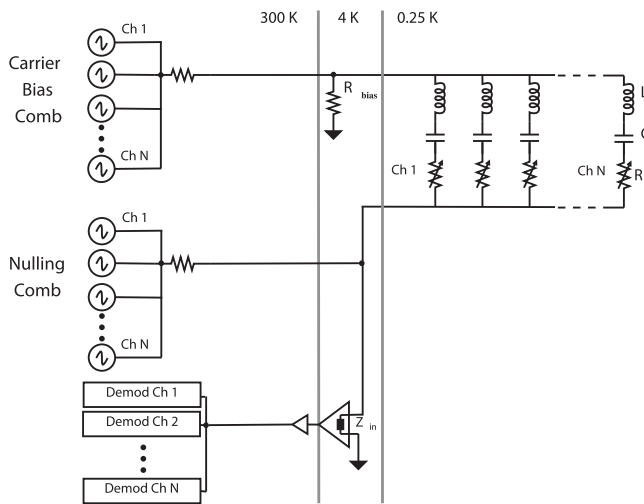


Figure 6. A schematic representation of an N channel FDM circuit. The TESs are in series with inductors and capacitors to form an LCR filter. All the TESs are in parallel with each other and a shunt resistor. The summed carrier bias tones travel down a single wire, interrogate their corresponding TES, and are summed together into a SQUID amplifier. Reprinted with permission from [61]. Copyright 2012, AIP Publishing LLC.

achieved 3 eV FWHM resolution or better at 5.9 keV for all the detectors except the unswitched row. Analysis methods were developed to determine the ideal matrix to deconvolve the data while minimizing crosstalk [58]. Larger Φ -CDM chips are under development and will be available for upcoming kilo-pixel arrays of x-ray TESs.

CDM retains much of the simplicity of TDM while eliminating the \sqrt{N} SQUID noise penalty. CDM can be implemented in a very compact footprint, i.e. under an overhanging absorber of an x-ray pixel [54]. So-called in focal plane multiplexing may enable very large sensor arrays in the future.

3.3. Frequency-division multiplexing

In FDM, distinct frequency tones are used to orthogonally encode a set of signals, see figure 3. In the current implementations of SQUID FDM at MHz frequencies [59, 60], the modulation is applied to the bias of the TESs and the signals from many TESs are summed into a single SQUID amplifier. As shown in figure 6, each TES in a unit block (column) is connected to an inductor and capacitor that define a frequency-specific resonance together with the TES resistance R . The LCR circuit selects a bandwidth around the target carrier frequency and filters out of band signals and noise. The resonances must be adequately separated in frequency space to prevent cross-talk. The signals for all the TESs in a given row are demultiplexed at room temperature using either an analog [61] or digital circuit [62]. Since the bandwidth of the readout can be limited to the same bandwidth as the sensor, FDM does not suffer noise aliasing from higher frequencies and does not have the \sqrt{N} noise penalty present in TDM.

A challenge of FDM is that all the signals and their carrier tones are summed and need to share the limited dynamic range of the measurement SQUID. Early versions of FDM extended the dynamic range of the SQUID by operating in a flux locked loop and applying a phase-shifted signal to cancel the carrier tones [61]. Still larger numbers of pixels per column can be achieved by employing feedback to cancel signals in the individual channels along with the carriers using baseband feedback (BBFB) [63] and digital active nulling (DAN) [64]. These techniques demodulate the carriers, identify the signals, create the necessary response to cancel carrier and signal at the SQUID and send this response as feedback. Such techniques can only work up to a maximum frequency set by time delays of the feedback circuit.

Another challenge is that the wiring before the amplifier must be carefully designed to reduce stray inductances and other series impedance that can affect the stability of the voltage-bias and cause crosstalk between channels [61]. The use of BBFB and DAN allow for larger inductances by suppressing the effective SQUID input impedance [64].

FDM is well established for the readout of TES bolometers. For example, the EBEX balloon instrument has 16 bolometers per readout chain between 0.4 and 1.2 MHz [65] and there are plans to move to bandwidths of a few MHz to multiplex 40 bolometers per readout chain for POLARBEAR-2 [66] and 160 bolometers per readout chain for the Safari instrument on SPICA [67]. While the first demonstration of high-resolution TES calorimeter multiplexing was performed with FDM [68], most subsequent TES calorimeter multiplexing has been performed with TDM and CDM. For example, the FDM multiplexing factor for gamma-ray TESs has not progressed beyond the two pixels described in [68]. Difficulties achieving similar energy resolution for AC-biased TESs as for DC, and the higher per pixel bandwidth of TES calorimeters compared to bolometers have been obstacles. However, recent developments suggest that some of the factors limiting the multiplexing factors achieved with FDM will be overcome.

There are plans to measure 40 x-ray TESs per readout SQUID for the ATHENA satellite mission [69] using FDM with BBFB and resonance frequencies up to 5 MHz. In preparation for ATHENA, much work has been focused on eliminating resolution degradation observed under AC-bias compared to DC [70, 71]. The cause of this degradation remains uncertain but one candidate originates in the nature of the resistive transition. As will be described in section 5, both the weak link and phase-slip models of the transition dictate that local regions of the $R(I, T)$ surface manifest increased noise. Under DC bias, these regions can usually be avoided [48]. Under AC bias, T is constant because the bias frequencies greatly exceed the maximum thermal response frequency but I varies with bias. As a result, even a quiescent pixel travels on the $R(I, T)$ surface and may encounter noisy regions of the transition. Nonetheless, resolution values achieved under AC bias continue to improve as does theoretical understanding [72].

FDM has a number of attractions including the absence of a \sqrt{N} SQUID noise penalty. Unlike in TDM and CDM, the

AC bias of the TESs allows individual bias levels to be set for each sensor. Since the detector signals are modulated to higher frequencies, some sources of low frequency noise are avoided. This property is shared with CDM. Also, modulation of the TES bias allows the use of reactive biasing [73], eliminating the additional power dissipation of the shunt resistor. Currently the power dissipation of the shunt resistor is not a limiting factor for TES instruments but could become important in the future for much larger arrays. FDM also has disadvantages. The LC filters needed for FDM occupy significantly more space than the LR filters used in TDM and CDM. The flux burden on the readout SQUID is highest for FDM necessitating more complicated feedback schemes. The use of AC TES biases complicates simple tasks like pixel characterization. Finally, achieving the same spectral resolution under AC bias as under DC is not routine and is presently a topic of research.

3.4. Microwave resonator based multiplexing

Two classes of microwave resonator based readout have received significant attention in the past decade due to their potential for readout of much larger arrays of sensors. The two techniques potentially offer total system bandwidths of 100s of MHz or even several GHz, compared to less than 10 MHz for time-, code-, and frequency-domain SQUID multiplexing as they are currently envisioned. The first class of microwave resonator based multiplexed readout uses MKIDs in which some part of the resonator is the sensing element. The signal of interest breaks Cooper's pairs causing a shift in resonance frequency and a drop in the quality factor that can be sensed by probing each resonator with a microwave tone. The second class is the microwave SQUID multiplexer, where the sensing element (i.e. a TES or magnetic calorimeter) is separate from the resonator and an intermediate SQUID couples the sensor response to the resonator. The SQUID response shifts the resonance frequency which can then be monitored in the same way as in MKID readout.

MKIDs were pioneered by the Zmuidzinas group at Caltech [74]. They are an attractive technology for large arrays of sensors because of the large potential readout bandwidth and the simplicity of their packaging. Most work to date has focused on long-wavelength astrophysics applications. For x-ray and gamma-ray applications, MKIDs have yet to show resolving powers that are competitive with TESs or magnetic calorimeters [19, 20]. One issue for x-ray and gamma-ray applications is how to design a MKID that combines high detection area with good energy resolution. Since excellent reviews of MKIDs exist [75], in the remainder of this section we will focus on microwave SQUID multiplexers.

Microwave SQUID multiplexing has the potential to combine the attractive features of MKID readout with proven TES x-ray and gamma-ray microcalorimeters. A schematic representation of one realization of microwave SQUID multiplexing is shown in figure 7. The current through each sensor is inductively coupled to either a dc or rf SQUID. Each SQUID is then coupled to a resonant circuit, such that a

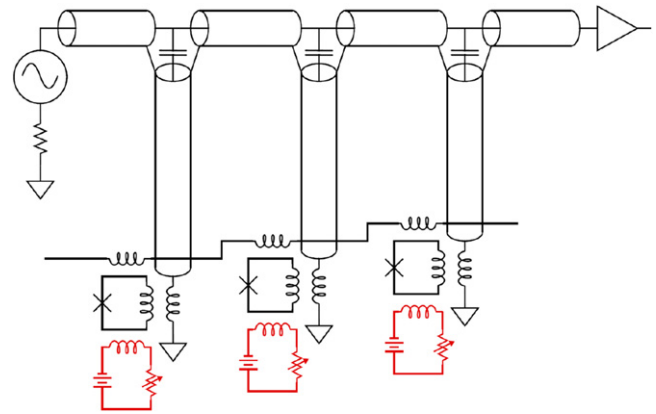


Figure 7. Schematic representation of a microwave SQUID multiplexing circuit. A rf SQUID is coupled to a microwave resonator such that a change in the inductance of the SQUID shifts the resonant frequency. Many resonators, each with a unique resonance frequency, are coupled to a common feed line. All resonators are read out simultaneously by applying a comb of probing frequencies to the feed line. The transmitted tones are amplified by a HEMT amplifier before reaching room temperature demodulation electronics. Figure courtesy of John A B Mates, National Institute of Standards and Technology.

change in flux in that SQUID shifts the resonant frequency of the corresponding resonator. All the resonant circuits are coupled to a common feed line and the response of the sensors is probed using a sum of microwave tones. The combined signals are measured by a single high bandwidth HEMT. At microwave frequencies, the resonant circuits can be fabricated from compact, low-loss components that are also compatible with typical SQUID fabrication processes. Microwave SQUID multiplexing has the potential to provide significantly more readout bandwidth than conventional techniques. This bandwidth can be used to multiplex larger numbers of sensors or alternatively allow each sensor to have a significantly higher bandwidth. A per sensor bandwidth increase could be useful for magnetic calorimeters in which the signal generation is intrinsically very rapid. Achieving high bandwidth per sensor could also be important for some proposed TES microcalorimeter experiments that operate at high count rates, such as at a high repetition rate x-ray free-electron laser, or where pileup rejection is critical, such as in neutrino mass measurements [76].

SQUIDs are typically operated in a feedback loop due to their periodic response curve. TDM, CDM, and low-frequency FDM multiplexing all incorporate feedback. Nonetheless, open loop operation of SQUIDs is possible and envisioned for microwave SQUID multiplexing. One approach is to flux-bias at a sensitive point of the SQUID response curve and to limit flux excursions to well below a flux quantum [77]. A more practical approach is to apply a rapidly varying signal to the SQUIDs in addition to the signal of interest so that the SQUID is modulated over the entire response curve [78–80]. For flux ramp modulation [80], a common ramp signal is coupled to all the SQUIDs. Assuming the modulation frequency is higher than the frequencies in the input signal, the input signal is extracted as a phase shift to the

demodulated signal. Flux ramp modulation has several important benefits. It linearizes the SQUID response without the need for feedback or a separate flux bias. A signal can be tracked over many flux quanta, increasing the usable dynamic range. Finally it modulates the SQUID signals to frequencies that are above the two-level system noise that often plagues other superconducting resonator based readouts [81]. Since the SQUID spends a fraction of its time in the insensitive portion of the response curve, there is a $\sqrt{2}$ noise penalty [80]. However, in most cases the benefits outweigh this small increase in the noise.

The microwave SQUID multiplexer was proposed and first demonstrated by Irwin *et al* [77]. The first demonstration used lumped element resonator circuits and dc SQUIDs and showed a flux noise of $\sim 0.5\mu\Phi_0/(\text{Hz})^{1/2}$. Since this work, there have been a number of other promising demonstrations in the range of a few GHz based on high Q lithographically fabricated resonators using both dc SQUIDs [79] and nearly dissipationless rf SQUIDS [82–85]. There have also been efforts to design microwave SQUID multiplexers for metallic magnetic calorimeters [86].

Recently, Noroozian *et al* [87] performed a two-pixel demonstration of microwave SQUID multiplexing where two gamma-ray TESs were readout simultaneously without significant degradation of the energy resolution. Using similar designs but with optimized coupling, the current noise referred to the input has been reduced to 17 pA/Hz^{1/2} [88], which should be suitable to read out most x-ray and gamma-ray TESs without resolution degradation. Kohjiro *et al* have also demonstrated low noise operation of a microwave SQUID multiplexer reporting 31 pA/(Hz)^{1/2} [85]. A variety of calorimetric instruments plan on using microwave SQUID multiplexers as their sensor readout including: SLEDGE-HAMMER [88], HOLMES [76], and ECHO [89]. The future of microwave SQUID readout looks extremely bright although significant work remains to be done on the room temperature electronics that must generate and demodulate the large number of microwave tones.

Finally, there is significant promise in hybrid multiplexing implementations where a combination of the different basis sets is used. For detectors that use a small fraction of the available bandwidth, i.e. many TES bolometers or slower microcalorimeters, these hybrid schemes have the potential to more efficiently use the available bandwidth. Hybrid multiplexing is common in the telecommunications industry, i.e. time-division multiple access (TDMA) and code-division multiple access (CDMA) in mobile phones. TDMA combines signals using TDM and then sends the combined signals over one of a larger number of frequency multiplexed channels. CDMA is similar but uses CDM instead of TDM. A demonstration of TDMA suitable for TESs was performed using a TDM first stage coupled to a second stage SQUID in a resonant circuit [90]. An especially efficient hybrid basis would be to use CDM as a first stage of a wide bandwidth microwave SQUID multiplexer [83]. A 256 channel CDM combined with a 512 channel microwave SQUID multiplexer would be capable of reading out 131,072 pixels. It would only

take eight of these systems to readout a megapixel array, enabling many new applications for microcalorimeters.

4. Pulse processing

The result of a photon or particle striking a microcalorimeter is an electrical pulse whose area and height are proportional to the deposited energy. Simple pulse processing approaches such as picking off the highest point of the pulse or integrating its area fail to use all the information contained in the data and thus do not produce the best resolving power. Under the assumptions that the signal and noise are stationary and that the pulse does not change shape with energy, it can be proven mathematically that the resolving power is maximized by convolving pulses with the optimal filter (Wiener filter) and using the height of the convolved pulses as an uncalibrated energy metric. The optimal filter is constructed from the average pulse shape and the noise power spectral density. Optimal filtering of pulses has been used for over two decades in microcalorimeters [91]. In this review, we focus on recent advances beyond the standard method. These advances are concentrated in two main areas; processing high-rate pulses that show significant pile-up and processing pulses that show a high degree of nonlinearity.

Many current and potential applications of microcalorimeters involve high photon event rates. In these applications, it is desirable to use piled-up pulses, i.e. pulses that fall on the tail of a previous pulse or that have another pulse in their tail. If these pulses are filtered with the typical optimal filter, the result gives a very poor estimate of the photon energy because the piled-up pulse shape does not match the average pulse shape. As a result, such events must be carefully removed from the data set. One way to utilize as many pulses as possible is to use short records that minimize the chances of pileup within a record. However, Doriese *et al* [92] have shown that short pulse records degrade resolution, even in the absence of pileup. The event grade technique [93] was developed for earlier microcalorimeters in order to balance energy resolution and photon throughput. Pulses are assigned to grades based on how close they occur in time to another pulse. Each pulse grade can have a filter whose length is appropriate for that pulse separation. The event grade technique will be used in the SXS instrument on Astro-H [94] and has been used to improve high rate data in TESs [95].

An alternative to optimal filtering in high rate scenarios was developed by Tan *et al* [96]. In this work, a running sum algorithm was used to extract pulse heights. While the running sum algorithm showed worse energy resolution compared to the optimal filter (about 10% worse for 3 eV FWHM resolution detectors), the effective record length can be very short and the algorithm can correct for a decaying baseline prior to the pulse of interest. Alpert *et al* [97] calculated the theoretical resolution of the running sum algorithm and showed that the observed degradation was consistent with the expected performance of this approach. For some applications, the increased throughput of the running sum filter may outweigh the degraded energy resolution. Also, the running

sum filter lends itself to implementation in firmware and has been demonstrated in real-time pulse processing [98].

Another approach to high rate pulse processing, proposed by Alpert *et al* [99], introduced the more general class of filters that are the optimal filter subject to constraints such as orthogonality to constants and orthogonality to exponentials. This work also used the noise auto covariance instead of the noise power spectral density to construct the optimal filter. With a filter that was orthogonal to both a constant and an exponential decay from a preceding pulse, Alpert *et al* showed a 45% higher output rate and better resolution for pulses with pile-up. However, the resolution limits are slightly worse for isolated pulses as constraints are added to the filter.

Perhaps the ideal approach to piled up data is to fit long time blocks that contain many pulses in one mathematical operation in order to extract their individual energies. Multi-pulse fitting is a method to perform maximum-likelihood fits for the amplitudes of more than one pulse in a record [100]. Like optimal filtering, it requires some amount of ‘training data’ to determine the noise power spectrum and the shape of the average pulse. Then after a pulse-finding pass, one can fit for the linear combination of pulses of the standard shape that best matches the observations. The cost of this computational fit is greatly reduced by approximating the noise as resulting from a low-order autoregressive-moving average model. The procedure has been used to good effect on data up to several hundred counts per second. However, sensor nonlinearity is an obstacle to MPF and all the algorithms just described. If the pulse shapes and gain curve of a sensor are altered by the presence of energy from a preceding pulse, then techniques that treat pile-up events as a linear combination of well-separated events will inevitably result in resolution degradation. Additional processing is needed to preserve energy resolution and throughput at high count rates in nonlinear devices.

Outside of the small signal limit, the response of TES sensors is intrinsically nonlinear both because of the transduction path (current is proportional to $V/(R + \Delta R)$ where ΔR is a resistance change proportional to deposited energy) and because of the shape of the $R(I, T)$ surface. For nonlinear pulses, the typical optimal filter is no longer ideal since the pulse shape changes with energy and the noise is not stationary. An empirical approach for highly nonlinear pulses was demonstrated by using different pulse templates at different energies [101, 102] and interpolating between templates. The potential of this method was demonstrated using nonlinear pulses generated from a model [103]. By using energy dependent filters, Fixsen *et al* [104] demonstrated the operation of TESs designed for optical photon detection well into the nonlinear regime with little loss of resolution.

The signal processing necessary to implement these algorithms for addressing nonlinearity can be significant. One option to reduce processing demands is to use a much smaller set of information to describe each pulse. Using principal components analysis, each pulse can be described using its projection onto a small number, i.e. 6 to 10, of components that contain the majority of the information about the pulses

and how they are different from each other [105]. Principle component analysis has demonstrated improved resolution relative to a standard optimal filter approach for x-ray TESs with highly nonlinear pulses [105]. Another option is to transform the signals from a current basis into a resistance basis which effectively adds weight to the temporal regions of the pulses that are otherwise suppressed by nonlinearity. Transformation to resistance space has improved performance on some nonlinear data sets [106]. Finally, another possibility to improve linearity of the TES response was recently proposed by van der Kurr *et al* [107] which is to use feedback to operate TESs with a nearly constant resistance instead of a nearly constant voltage.

Improved knowledge of the nature of nonlinearity in TESs is desirable to improve the processing of nonlinear pulses. Shank *et al* [108] used a phenomenological model of the resistive transition to create pulse templates that were used to optimally filter pulses well into the saturation region. As we will see in section 5.4, new physics-based models of TESs also enable large-signal limit models of the detector response. If information from these large-signal limit models is incorporated into the pulse processing, for example to build templates for multi-pulse fitting, optimum energy resolution may be obtainable even in the most challenging high count rate, nonlinear response scenarios.

5. TES physics

Until recently, there were no plausible physical models to describe the behavior of the resistance of TESs when they were biased in the superconducting transition. The resistance in a TES is not only a function of temperature, but also a function of current in the film. Therefore, any model that attempts to describe the resistance of the TES must include a mechanism for the current dependence. Two such models have been proposed, one based on Josephson junction-like weak-link behavior and the other based on intermediate resistance states formed by phase-slips lines (PSLs). These models were developed to describe distinctly different observations and are believed to describe the resistive mechanism in different regimes based on device size and materials properties. We will first review the TES physics relevant to our discussion of the various resistance models. We will then describe the weak-link behavior observed in TESs and the measurements that motivated it, and then discuss the two-fluid and phase-slip models and how they explain other observed behavior in TESs. After reviewing the TES resistance models we will briefly calculate some device parameters in order to roughly compare the models. Finally we will demonstrate part of the utility of these models by calculating pulse shapes in the large signal limit.

5.1. TES theory review

In this section we will give a brief review of the standard theory and parameter definitions used in modeling the behavior of TESs in order to frame the subsequent discussion. If

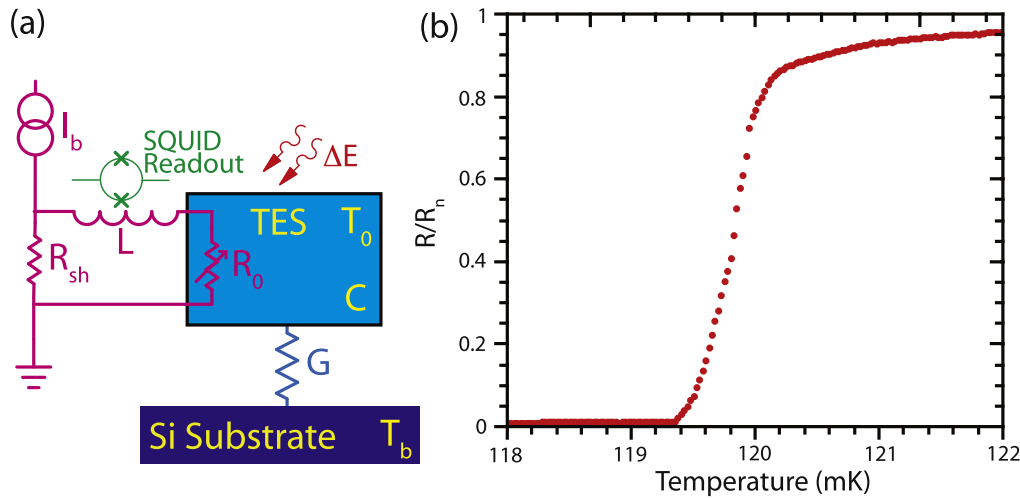


Figure 8. (a) Schematic representation of the coupled electrical and thermal circuits of a TES. (b) A typical measurement of the resistance of a TES across the superconducting to normal transition. The resistance (in units of R_n) was measured from the response to a small ac excitation current.

the reader is interested in a more extensive review of TES models in the small-signal limit, we suggest the 2005 seminal review of TESs by Irwin and Hilton [8].

TESs operate in the superconducting transition between the normal and superconducting state, see figure 8(b). When biased in the transition small changes in temperature can cause large changes in resistance making TESs a very sensitive thermometer over small ranges of temperature. Since the 1995 proposal by Irwin [5], TESs have been primarily operated under a stiff voltage bias and are read out using a SQUID amplifier. This mode of operation has a number of advantages over current biased TESs readout with a voltage amplifier as was common in the early days of TESs. Two important results of voltage bias are negative electrothermal feedback and the compatibility with SQUID amplifiers suitable for multiplexing large arrays. The advantages of electrothermal feedback include faster detector response, improved linearity, and less stringent demands on device uniformity.

Voltage bias is typically achieved by placing the TES in parallel with a shunt resistor (R_{sh}) that is much smaller than the resistance of the TES at its operating point. A schematic representation of the TES bias circuit is shown in figure 8. It is often reasonable to assume that the voltage bias is completely stiff and to transform the circuit into its Thevenin equivalent circuit with a voltage bias (V) and equivalent resistance $R_L = R_{sh} + R_p$, where R_p is the parasitic resistance in parallel with the shunt that is not part of the TES (not responsive to temperature). Then the equation describing the electrical behavior of the TES is [5–8],

$$L \frac{dI}{dt} = V - IR_L - IR(T, I), \quad (1)$$

where L is the sum of all the inductance on the TES's branch of the bias circuit.

In its simplest version, the TES is assumed to have a heat capacity (C) connected weakly through a thermal conductance (G) to a temperature bath (T_b), see figure 8(a). Both C and G

can depend on temperature. Usually it is assumed the T does not change significantly during the operation of the TES and the temperature dependence of C and G on T are ignored. We can then derive the differential equation describing the thermal behavior as the difference between the heat generated by the sum of the signal power (P) and Joule power (P_J) and power lost due to heat flow through the thermal conductance to the bath (P_b) [5–8]

$$C \frac{dT}{dt} = -P_b + P_J + P. \quad (2)$$

For TESs on thin membranes, power flow to the heat bath is usually assumed to have a power law dependence

$$P_b = k(T^n - T_b^n), \quad (3)$$

where n is between 3 and 4 for standard TES materials and $k = G/n(T^{n-1})$ where G is the thermal conductance ($G = dR_b/dT$). Multiple thermal body models [7, 109] are sometimes needed in order to accurately describe more complex devices, i.e. an attached bulk absorber [46].

Once models for the resistance in the transition and for thermal conductance are given, equations (1) and (2) can be solved to give the dynamic behavior of a TES. Later we will show examples of numerical solutions to these equations. However, further simplifications are possible by linearizing the differential equations about the steady state parameters R_0 , T_0 , and I_0 and operating in the small signal limit. In practice, most calorimeters are operated outside of this limit in order to maximize dynamic range and improve energy resolution. Put simply, if the largest photon energy of interest only causes a small deviation of the current from the operating point, a smaller heat capacity could likely be used to improve resolution. Despite the limitations of the small signal limit, the simplifications afforded by linearizing the equations make it possible to have reasonable analytic equations for the temperature and current as a function of time and are invaluable in understanding how to design and operate a TES. Additionally, the linearization of the resistance allows use of the

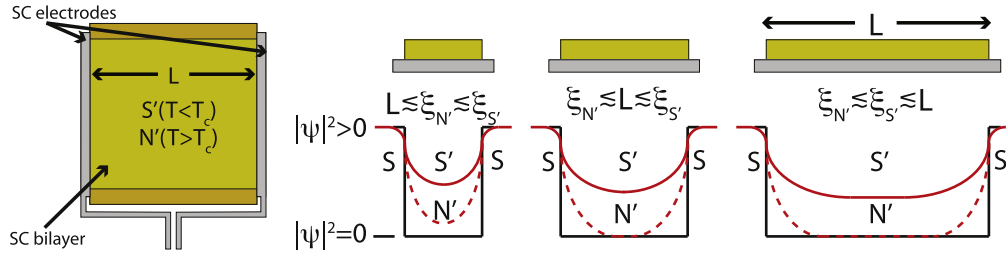


Figure 9. Schematic representation of a bilayer TES showing the modulus squared of the superconducting order parameter for SS'S ($T < T_c$ solid red line) and SN'S ($T > T_c$ dashed red line) in three different length TESs.

equations without understanding the global behavior of resistance across the $R(I, T)$ surface.

A linear first-order expansion of the resistance about the operating point gives [7, 8]

$$R(I, T) \approx R_0 + \left. \frac{\partial R}{\partial T} \right|_{I_0} \delta T + \left. \frac{\partial R}{\partial I} \right|_{T_0} \delta I, \quad (4)$$

where $\delta T = T - T_0$ and $\delta I = I - I_0$. It is customary to define the unitless logarithmic temperature sensitivity

$$\alpha_I = \left. \frac{\partial \log R}{\partial \log T} \right|_I = \frac{T}{R} \left. \frac{\partial R}{\partial T} \right|_I, \quad (5)$$

and the unitless logarithmic current sensitivity

$$\beta_I = \left. \frac{\partial \log R}{\partial \log I} \right|_T = \frac{I}{R} \left. \frac{\partial R}{\partial I} \right|_T. \quad (6)$$

With these definitions, equation (4) becomes

$$R(I, T) \approx R_0 + \alpha_I \frac{R_0}{T_0} \delta T + \beta_I \frac{R_0}{I_0} \delta I. \quad (7)$$

Similar expansions are necessary for P_b and P_I in order to derive the coupled linear equations that are often useful for understanding, for example, if the TES is electro-thermally stable, to predict the effect of the various noise sources, or to directly study the dynamic behavior of the current and temperature when a photon is absorbed. The use of these equations is well established [8] and therefore not a topic of this review. Instead the following sections focus on recent advances in understanding the physics of the superconducting transition in TESs and the implications new models have on device design. The connection between resistance models and typical characterization of TESs is made through how α_I and β_I depend on the relevant TES parameters. Therefore the predictions that resistance models make for α_I and β_I are relevant starting points for evaluating their applicability to real devices.

5.2. Transition models

5.2.1. Weak-link behavior. Weak-link behavior in TESs was first reported by Sadleir *et al* [110] in Mo-Au TESs with Mo/Nb leads. They observed an exponential dependence of the critical current of the TES on the length between the Mo/Nb leads from 8 to 290 μm . The critical current versus

temperature data were fit using an expression for I_c that was derived from Ginzburg–Landau (G–L) theory [110] as

$$I_c(T, L) = \frac{F}{\xi} \exp\left(\frac{-L}{\xi}\right), \quad (8)$$

where F is a combination of parameters and is nearly independent of temperature for temperatures well below the critical temperature of the leads (T_{cL}). In this case, ξ is the superconducting coherence length defined as

$$\xi(T) = \xi_i \frac{1}{|T/T_{ci} - 1|^{1/2}}, \quad (9)$$

where ξ_i is an intrinsic coherence length, and T_{ci} is the intrinsic transition temperature of the weak link in the absence of leads. The best fit to the data in [110] was for $\xi_i = 738$ nm. Even more striking than the weak-link temperature dependence of critical current was the observation of a Fraunhofer-like dependence of the critical current on magnetic field. Later, these findings were extended to devices with normal-metal noise mitigating structures [111]. Since these initial efforts, a major obstacle has been understanding how these observations of weak-link behavior in TES at the edge of the purely superconducting state affect the behavior of devices biased in the transition.

A superconducting weak link is a weak electrical contact of direct (non-tunneling type) conductivity between superconducting electrodes [112]. Due to the proximity effect, the order parameter (ψ) of the superconducting electrodes extends into the weak link, decaying exponentially over a distance of the coherence length (ξ). A schematic view of the weak-link behavior in TESs is depicted in figure 9. The plots show the magnitude of ψ starting in the higher T_c leads and moving across the TES film giving either SS'S ($T < T_c$ solid red line) or SN'S ($T > T_c$ dashed red line) depending on the state of TES film. If $\xi \lesssim L$ then the order parameter does not go to zero and supercurrent can traverse the weak link. When $T < T_c$, the TES bilayer thin film is in the superconducting state (S') and the coherence length is $\xi_{S'}$. When $T > T_c$, the TES bilayer thin film is in the normal state (N') and the coherence length is $\xi_{N'}$. Except when $L \gg \xi$, the critical current of a weak link depends on L .

Based on these insights, Kozorezov *et al* [113] proposed applying to TESs the resistively shunted junction model (RSJ) commonly used for weak-link Josephson junctions [112]. The RSJ model assumes that the resistance is determined by the interaction of the superconducting leads with the intervening

TES film. Kozorezov *et al* base their specific implementation of the RSJ model on a model developed by Coffey *et al* [114] that describes quantum corrections to the standard Brownian motion of a particle in a tilted washboard potential in the presence of thermal fluctuations. In the classical limit, the resistance of the weak link is

$$R(T, I) = R_n \left(1 + \frac{1}{x} \Im \left[\frac{I_{1+i\gamma x}(\gamma)}{I_{i\gamma x}(\gamma)} \right] \right), \quad (10)$$

where R_n is the normal resistance, $x = I/I_c(T)$, $I_c(T)$ is the critical current, and $\gamma = (\hbar I_c(T))/(2ek_B T)$ is the ratio of Josephson coupling energy to thermal energy. $I_{1+i\gamma x}(\gamma)$ and $I_{i\gamma x}(\gamma)$ are modified Bessel functions $I_\nu(z)$ of complex order ν and real variable z . For typical TESs, γ is large near the maximum I_c , e.g. $\gamma \approx 10^5$ at $I_c = 1$ mA and $T = 100$ mK, and goes to zero as I_c goes to zero. The α_I and β_I are calculated as [113]

$$\alpha_I = -\frac{\gamma}{x} \frac{\partial \ln I_c}{\partial \ln T} \frac{R_n}{R} \Im \left[\frac{I_{-1+i\gamma x}(\gamma) I_{1+i\gamma x}(\gamma)}{I_{i\gamma x}^2(\gamma)} \right], \quad (11)$$

$$\beta_I = \frac{R_n}{R} \left(1 - 2\Re \left[\frac{\int_0^\gamma I_{i\gamma x}(z) I_{1+i\gamma x}(z) dz}{I_{i\gamma x}^2(\gamma)} \right] \right) - 1. \quad (12)$$

For the scenario where the TESs are small and the T_c of the leads is an order of magnitude larger than the TES, Kozorezov *et al* [115] suggest the use of the Usadel formalism to describe the temperature dependent critical current. For a given geometry and materials, the I_c is calculated numerically and then used in the RSJ model. Due in part to the difficulty of these calculations, the RSJ model in this form has only recently been applied to real devices [72].

Bennett *et al* [116] pointed out that equation (10) has natural limits based on the limits of γ , which parameterizes the effect of thermal fluctuations. In the limit where $\gamma \rightarrow \infty$, the zero-temperature limit, the RSJ model has a simpler form [117]. For $I > I_c$, the voltage across the TES is

$$V = R_n (I^2 - I_c(T)^2)^{1/2}, \quad (13)$$

and the resistance in terms of current is

$$R(T, I) = R_n \left(1 - \left(\frac{I_c(T)}{I} \right)^2 \right)^{1/2}. \quad (14)$$

The RSJ resistance at finite temperature is bounded by R_n on the high side and by equation (14) on the low side. α_I can be calculated by rearranging the partial derivative $\alpha_I = T/(RI) \partial V / \partial T$, and then taking the derivative of equation (13) at constant current,

$$\alpha_I = -\frac{R_n^2}{R^2} \frac{I_c(T)}{I^2} T \frac{\partial I_c}{\partial T} = -\frac{R_n^2}{R^2} \frac{I_c(T)}{I^2} \frac{\partial \ln I_c}{\partial \ln T}. \quad (15)$$

β_I can be calculated by rearranging the partial derivatives as $\beta_I = 1/(R) \partial V / \partial I - 1$ and taking the derivative of

equation (13) at constant temperature

$$\beta_I = \frac{R_n}{R} \frac{1}{\left(1 - \left(\frac{I_c(T)}{I} \right)^2 \right)^{1/2}} - 1 = \left(\frac{R_n}{R} \right)^2 - 1. \quad (16)$$

Numerical evaluation of equations (11) and (12) show that, at any given value of I/I_c , equations (15) and (16) give the maximum values of α_I and β_I in the RSJ model. Bennett *et al* [116] also showed that the minimum values for α_I and β_I given in equations (11) and (12) are found in the long junction limit [112] and are the same as in the two-fluid model. Then instead of equation (14) the resistance is given by

$$R(T, I) = R_n \left(1 - \left(\frac{I_c(T)}{I} \right) \right). \quad (17)$$

In this limit α_I and β_I are given by [118]

$$\alpha_I = -\frac{R_n}{R} \frac{I_c(T)}{I} \frac{\partial \ln I_c}{\partial \ln T}, \quad (18)$$

and

$$\beta_I = \frac{R_n}{R} - 1, \quad (19)$$

assuming that I_c is not a function of current. The temperature dependence of I_c must be known to evaluate α_I so it is more straightforward to compare β_I to data. This comparison is postponed until after the other models have been reviewed.

Extensions to equations (15) and (16) for magnetic field are described in Smith *et al* [119]. The inclusion of magnetic field is accomplished by assuming that the only effect of the field is to modulate $I_c(T, B)$. For devices with no additional normal-metal features, i.e. normal metal banks or bars, the modulation of I_c is the standard Fraunhofer pattern typical for square Josephson junctions [120, 121]

$$I_c(\Phi) = I_c(0) \left| \frac{\sin(\pi\nu)}{\pi\nu} \right|, \quad (20)$$

where I_{c0} is the zero field critical current and $\nu = \Phi/\Phi_0$ where Φ is the flux through the junction and $\Phi_0 = 2.07 \times 10^{-15}$ Wb is the flux quantum. For devices with non-uniform tunneling current distributions Smith *et al* [119] have suggested using the 'one-parameter' model proposed by Barone and Paterno [122],

$$I_c(\nu) = I_{c0} \frac{\chi^2}{\chi^2 (\pi\nu)^2} \left| \frac{\pi\nu \sin(\pi\nu)}{\chi \tanh(\chi)} + \cos(\pi\nu) \right|, \quad (21)$$

where $\chi = aw/2$, w is the lateral dimension across the junction, $a = J(\pm w/2)/J(0)$ is the ratio of the current density at the edge of the junction ($x = \pm w/2$) to that at the center ($x = 0$) and

$$J(x) = J_0 \frac{\cosh(ax)}{\cosh(aw/2)}. \quad (22)$$

Using equation (21) with $a = 4.4$, Smith *et al* [119] were able to fit their measured I_c data as a function of applied magnetic field for their 140 μm by 140 μm Mo-Au TES with normal-metal features.

In order to include the self-field effects created by the non-uniform flow of current across the TES [10], Smith *et al* [119] use an empirical relation to describe the change in field as a function of the change in current and temperature of the TES

$$\Delta B(I, T) = g_I I + g_T (T - T_{c0}), \quad (23)$$

where g_I and g_T are phenomenological constants. The total field is then $B = B_{\text{ext}} + \Delta B(I, T)$. They then go on to derive α_I and β_I based on the RSJ model resistance in equation (14) using the self-field parameters from equation (23) and the I_c dependence from equation (21). This model predicts discontinuities at the minimum of the $I_c(B)$ curve when the slope of I_c with respect to B changes direction. Features similar to this have been observed in measured values of α_I and β_I .

When the predicted α_I and β_I are compared to data without any self-field effects, they are an order of magnitude larger than the measured values. The modulation of I_c with magnetic field could explain this discrepancy over small regions of bias but does not explain the difference across the whole transition. A number of possibilities are proposed for the source of the discrepancy, including non-equilibrium superconductivity, an incorrect current–phase relationship in the RSJ model, or charge imbalance from quasiparticle recombination [119]. If instead of equation (14), equation (17) was used for the resistance, measured and predicted values are in much better agreement. However, in this limit of the RSJ model, the $I_c(B)$ should be approaching the behavior predicted for a 2D superconducting film rather than a weak-link junction. It could be possible that as the film becomes more resistive there is a gradual transition to a two-fluid like model without the junction-like behavior [116]. Resolving the discrepancy between the predicted and measured α_I and β_I is an important future issue for weak-link TES models.

Other groups have reported observing weak-link behavior. Gottardi *et al* [123] reported an enhancement of the modulation of I_c with magnetic field under AC bias compared to DC bias in their low-G bolometer using a 50 by 50 μm Ti/Au TES with $R_n = 98 \text{ m}\Omega$ and $T_c = 85 \text{ mK}$ and Nb leads and later showed good agreement between equation (10) for the real and imaginary part of an IV curve of an ac biased TES [72]. Wang *et al* [124] have studied the proximity effect in TESs with additional superconducting structures. Another group has experimented with structures to reduce the proximity effects on T_c [125].

Finally, there has been some surprise and confusion around the long intrinsic coherence lengths, labeled earlier as ξ_i , necessary for the observed behavior to be attributed to a Josephson weak-link effect. However, it must be understood that the proximity effect due to the leads plays a role in extending the weak-link effect well beyond the intrinsic coherence length of the material. ξ can then be much larger than the coherence length that is the characteristic length from standard G–L theory (ξ_{GL}) and also different than the Pippard coherence length (ξ_0) [126]. Near T_{ci} , ξ_{GL} can be related to ξ_0

though BCS theory to give [126]

$$\xi_{\text{GL}}(T) = 0.74 \frac{\xi_0}{(1 - T/T_{\text{ci}})^{1/2}}, \quad (24)$$

in the clean limit and

$$\xi_{\text{GL}}(T) = 0.855 \frac{(\xi_0 \ell)^{1/2}}{(1 - T/T_{\text{ci}})^{1/2}}, \quad (25)$$

in the dirty limit, where ℓ is the mean free path. Typical values quoted for different materials are either ξ_0 or the zero temperature value of ξ_{GL} , which both tend to be much smaller than ξ defined in equation (9). ξ (as defined in equation (9)) is much closer to the definition of the effective coherence length in the weak-link literature.

To analyze the weak-link Josephson effect in an SS'S junction at arbitrary temperatures requires solutions to the Usadel equations. However, there are a number of reasonable approximations in various limits. For long lengths and $T \geq T_{\text{ci}}$ the Usadel formalism gives an exponential dependence in $-L/\xi^*$ [112, 127]. The I_c is

$$I_c(T, L) = I_{c0} V^* \frac{L}{\xi^*} \exp\left(\frac{-L}{\xi^*}\right), \quad (26)$$

where ξ^* is the effective decay length and I_{c0} is a grouping of all the constants with units of current. In the limit of an SNS junction where $T_{\text{ci}} = 0$ [128]

$$\xi^* = \xi_N \sqrt{\frac{T_{\text{cL}}}{T}}, \quad (27)$$

$$V^* = \frac{32T\Delta^2}{T_{\text{cL}} \left[\pi k_B T + \Delta^* + \sqrt{2\Delta^* (\pi k_B T + \Delta^*)} \right]^2}, \quad (28)$$

where $\Delta^* = \sqrt{(\pi k_B T)^2 + \Delta^2}$, and ξ_N is the intrinsic coherence length of the weak-link material above T_{ci} . For a long SNS junction, the effective coherence length is larger than the intrinsic coherence length by a factor $\sqrt{T_{\text{cL}}/T}$. For arbitrary T_{ci} Kupriyanov *et al* [129] give an expression for ξ^* with an accuracy better than 3%

$$\xi^* = \xi_N \sqrt{\frac{T_{\text{cL}}}{T} \left[1 + \frac{\pi^2}{4} \ln^{-1} \left(\frac{T}{T_{\text{ci}}} \right) \right]}. \quad (29)$$

Then for $T \geq T_{\text{ci}}$, the I_c of an SS'S junction is well approximated by equation (26) with equations (28) and (29). In order to compare to data, we need a reasonable approximation of the gap in the leads. For isotropic s-wave superconductors, a good approximation is [130]

$$\Delta(T) = 1.76 \tanh \left(\frac{\pi}{1.76} \sqrt{\left(\frac{T_{\text{cL}}}{T} - 1 \right)} \right). \quad (30)$$

Now we can address the question of how this compares to the coherence lengths observed by Sadleir *et al* [110]. For T

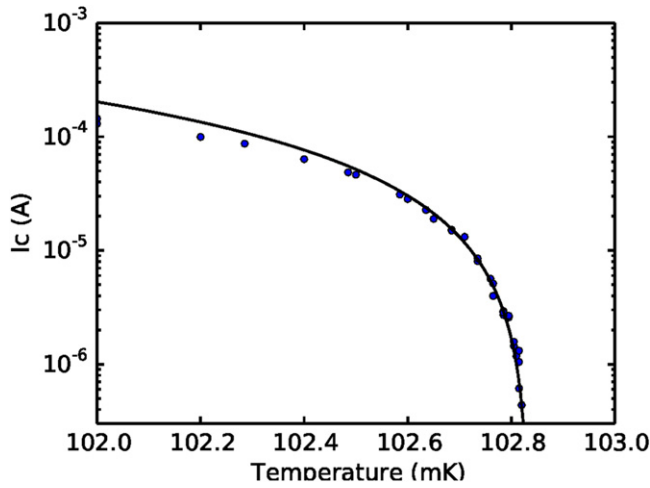


Figure 10. Measured I_c (blue points) as a function of T for a 400 μm Mo-Cu TES. The black line is a fit to equation (33) giving $I_{c0} = 270$ mA and $T_c = 102.83$ mK.

close to T_{ci} , equation (29) can be approximated as

$$\xi^* = \frac{\pi}{2} \xi_N \sqrt{\frac{T_{cL}}{T}} \frac{1}{(T/T_{ci} - 1)^{1/2}}. \quad (31)$$

Comparing equations (31) and (9) we find that

$$\xi_i = \frac{\pi}{2} \sqrt{\frac{T}{T_{ci}}} \xi_N. \quad (32)$$

Therefore, in this notation ξ_N , or ξ_0 if the barrier material is a superconductor, is the intrinsic property of the material while ξ_i (from equation (9)) includes the enhancement due to the larger superconducting gap of the leads. When equations (26), (28), and (29) are over plotted on the $I_c(T)$ data from [110], it agrees with both the data and equations (8) and (9) over the range of lengths. From this we can conclude that the value reported in [110] ($\xi_i = 738$ nm) would correspond to an intrinsic coherence length of the MoAu bilayer of 97 nm.

5.2.2. The two-fluid model and phase-slip behavior. Large classes of TESs do not show signs of the weak-link behavior described in the previous section. The exact difference between these devices and the devices that show weak-link behavior will be described in detail in the following section, but in general they tend to be larger, have a smaller difference between T_{cL} and T_{ci} , and have more normal-metal noise-mitigating features. These non-weak-link devices do not display either of the features that distinguish the weak-link devices. They do not show a periodic modulation of I_c with magnetic field, and near the transition have an I_c that is well described by G–L prediction for the critical current of a thin-film superconductor.

Figure 10 shows the measured I_c as a function of temperature for a NIST Mo-Cu 400 μm TES optimized for gamma-ray spectroscopy up to 200 keV [40]. The black line

is the G-L critical current that has the standard form

$$I_c(T) = I_{c0} \left(1 - \frac{T}{T_c}\right)^{3/2} \quad (33)$$

where I_{c0} is the value of I_c at zero temperature. At temperatures more than a few milliKelvin below T_c , equation (33) overestimates the I_c since it does not include the non-uniform current distribution that occurs in wide films. Since there is no evidence of an exponential dependence on T or any deviation from G–L behavior for a 2D superconducting film, it seems reasonable that there is no weak-link behavior.

The I_c versus magnetic field has been measured for the same devices and there is no evidence of any Fraunhofer-like behavior indicative of the weak-link behavior in TESs. For most of the devices, the effect of magnetic field on critical current is most closely modeled as

$$I_c(B) = I_{c0} \left(1 - \left(\frac{H}{H_c}\right)^2\right), \quad (34)$$

where H_c is the critical field. For smaller devices (≈ 125 μm) with no additional metal features, the dependence starts to instead approach

$$I_c(B) = I_{c0} \left(1 - \left(\frac{|H|}{H_c}\right)\right). \quad (35)$$

Without evidence of either effect typical for weak-link TESs, there is no reason to believe that the RSJ model is appropriate for these devices. The RSJ based models tend to seriously overestimate the transition parameters (α_I and β_I) in these devices. The important question arises, what is the mechanism for resistance in the TESs that do not show any obvious weak-link behavior.

A model to describe the resistance in the transition was proposed in 1998 by Irwin *et al* [131], based on the two-fluid model as a simplification of the model for phase-slip centers proposed by Skocpol–Beasley–Tinkham (SBT) [132]. This two-fluid model was used to derive the sensitivity of the transition assuming a G–L temperature dependence for I_c , equation (33). The resistance in the two-fluid model is

$$R(I, T) = c_R R_n \left(1 - c_I \frac{I_c(T)}{I}\right), \quad (36)$$

where c_R and c_I are the phenomenological two-fluid parameters. The total resistance can be viewed as the normal resistance in parallel with the resistance carried in the superconducting channel. Written in this form, its close similarity to the RSJ model is obvious. If $c_R = 1$ and $c_I = 1$, then the two-fluid model has the same form as equation (17), and equation (14) is the square root of the sum of the squares of the same two terms [116].

More than a decade later, Bennett *et al* [118] derived α_I and β_I for the two-fluid model under voltage bias and compared it to measurements. The derived α_I and β_I for the two-fluid model assuming G–L dependence for $I_c(T)$ are

given by [118]

$$\alpha_I = \frac{3}{2} c_I c_R \frac{R_n I_{c0} T_0}{R_0 I_0 T_c} \left(1 - \frac{T_0}{T_c} \right)^{1/2}, \quad (37)$$

assuming c_I and c_R are not a function of T , and

$$\beta_I = c_R \frac{R_n}{R_0} - 1, \quad (38)$$

assuming that I_c and c_R are not a function of current.

This model showed significant promise by reproducing much of the general behavior of the IV characteristic as a function of bath temperature and α_I and β_I as a function of current and bias point. A few groups have compared the predictions of the two-fluid model to data with reasonable success [118, 133, 134]. The two-fluid parameters give the model much flexibility. However a true physical model of the resistance must describe the nature of these parameters. Over any small section of bias, suitable parameters can be found to fit measured data [116]. However the value c_R must vary across the transition to describe IVs and measured data across a larger range of bias points. The two-fluid model is very useful for developing understanding over small regions and its simplicity lends itself well to helping understand general behavior. For example, it is useful for understanding why α_I and β_I increase low in the transition, see figure 14.

Since its proposal by Irwin *et al* [131], the physical justification for the two-fluid model has been the concept of PSLs. PSLs are two-dimensional manifestations of the concept of phase-slip centers (PSCs) proposed by SBT [132] to describe the step-like IV structures observed in thin tin whiskers. A number of groups have observed that a low dimensional superconducting whisker or nanowire that exceeds its critical current (I_c) is not driven directly from the superconducting state to the normal state as was initially predicted. Instead, the IV curve shows regions of constant resistance in between a series of regular voltage steps [126]. As predicted by the depairing current, I_c is the point of the first onset of voltage across the device. Between steps, the differential resistance is an integer multiple of the resistance after the first jump. This behavior has been shown in numerous experiments [135–138], to result from phase-slips, where the phase of the superconducting order parameter is increasing at different rates on the two sides of a spatially localized region.

In the phase-slip process, the local super-current (I_s) is oscillating in time at the Josephson frequency [126]. The oscillation is caused by the build up and subsequent collapse of the electric field inside the superconductor. At a bias current above the local critical current (I_c), an electric field appears locally since the zero voltage state is no longer possible above I_c . The Cooper pairs are accelerated by the electric field until the super-current (I_s) is above I_c . When I_s exceeds I_c the order parameter is driven to zero. The total current (I) remains constant throughout the process requiring that all the current is briefly carried by the normal current as quasiparticles. The super-current is reestablished and the cycle repeats. Averaged over time, the I_s in the phase-slip

region is some fraction of the total critical current $\bar{I}_s = c_I I_c$. The difference between the total current and the time-averaged super-current, $I - \bar{I}_s$, is carried by the quasiparticles. The length scale on either side of the phase-slip, where the current is carried by the quasiparticles, is Λ_{Q^*} . Λ_{Q^*} has been shown to have a weak temperature dependence $\Lambda_{Q^*}(T) \approx \Lambda_{Q^*}(0) / (1 - T/T_c)^{1/4}$ [139, 140], that is more relevant in TESs since they are operated close to T_c . Swetz *et al* [10] determined Λ_{Q^*} in a Mo-Cu bilayer near T_c to be in the range of 3 μm to 6 μm .

The voltage across an isolated PSC was given within the SBT model as

$$V = 2\Lambda_{Q^*} R_n (I - c_I I_c) / L, \quad (39)$$

where L is the length of the device and R_n is the normal resistance of the device. The parameters of the two-fluid model were written in order to correspond directly to the parameters in equation (39), with $c_R = 2\Lambda_{Q^*}/L$. The transition from one phase-slip to a second would then cause c_R to double. As the current increases, the number of phase-slips (n_{ps}) increases and the c_R of the two-fluid model increases. This increase is consistent with measured data. In order to apply the concept of phase-slips to TESs, a model is needed that predicts the current and temperature dependence of the transitions between different numbers of phase-slips.

A simple model is shown schematically in figure 11, where the total current and its various components are shown as a function of position across the film. In figure 11(a), for a given total current there are three PSLs, shown by the black arrows, and \bar{I}_s does not exceed I_c . When the bias current is increased (b) the portion of current carried by \bar{I}_s exceeds I_c at a few points, indicated by the red arrows. It then becomes favorable for the creation of a new PSL (c), so that once again, \bar{I}_s remains below I_c .

This model was first proposed by Tinkham [141] for the case of multiple interacting PSCs in a perfectly uniform one-dimensional superconductor. The voltage drop across n_{ps} equally spaced phase-slips in a device of length L is

$$V_n = \frac{2n_{\text{ps}}\Lambda_{Q^*}}{L} R_n (I - c_I I_c) \tanh \left(\frac{L}{2n\Lambda_{Q^*}} \right). \quad (40)$$

In this model, \bar{I}_n decays exponentially away from a phase-slip, and \bar{I}_s is largest midway between two phase-slips. Assuming equally spaced phase-slips, the maximum current for n_{ps} is

$$I_{\text{max},n} = I_c \frac{\cosh \left[L / \left(2(n_{\text{ps}} + 1)\Lambda_{Q^*} \right) \right] - c_I}{\cosh \left[L / \left(2(n_{\text{ps}} + 1)\Lambda_{Q^*} \right) \right] - 1}. \quad (41)$$

This expression does not take into consideration the proximity effect caused by the increased order parameter due to the leads, as was discussed in the previous section. A more accurate model would modify equation (41) to take these effects into consideration.

Bennett *et al* [142] adapted Tinkham's results for uniform one-dimensional current-biased whiskers to

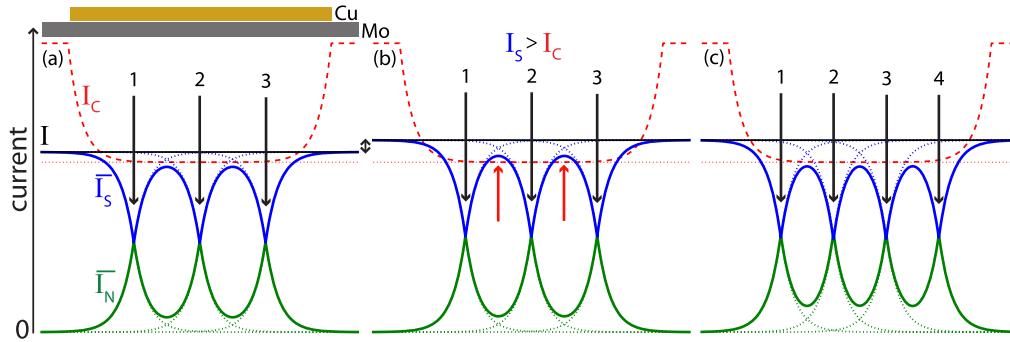


Figure 11. Schematic depiction of the conditions that cause the formation of a new PSL. The total bias current (black) is the sum of \bar{I}_S and \bar{I}_N . In (a) there are three PSLs and \bar{I}_S does not exceed I_c . In (b) the total current is increased causing \bar{I}_S to exceed I_c . This causes the creation of a new PSL (c) allowing \bar{I}_S to once again remain below I_c .

voltage-biased two-dimensional films [143]. To voltage bias the superconducting film, it is placed in parallel with a shunt resistor R_{sh} . The total current (I_t) divides between R_{sh} and the TES such that the voltage drops are equal,

$$(I_t - I)R_{sh} = \frac{2n_{ps}A_Q^*}{L}R_n(I - c_I I_c(T))\tanh\left(\frac{L}{2n_{ps}A_Q^*}\right). \quad (42)$$

In [142], it was demonstrated that when this criteria is combined with the condition of power balance there are regions of bias where there is no simultaneous solution to both equations. Stated another way, the solution falls in between two integer number of PSLs. Since only integer numbers of PSLs can exist, the film is forced to one state or the other based on initial conditions, but can possibly switch back and forth between the states due to current or temperature noise. Bennett *et al* [142] demonstrated that the predicted difference between the two states is consistent with the observation of regions of bi-stability in IV curves. It is also hypothesized that switching between different number of PSLs could account for the observation of telegraph noise at certain bias voltages in some TESs [144] and bi-stability at given resistances as observed in pulses [34].

Magnetic field is incorporated into the two-fluid and PSL models for the TES in the same way it has been incorporated into the RSJ model [119] via the critical current dependence, $I_c(T, I, B)$. However, for the larger devices where the two-fluid and PSL models are appropriate, the TESs tend to be much less sensitive to field, equation (34), and do not show any local minimums in $I_c(B)$. So the general result of including magnetic field in a two-fluid or PSL models in this way is similar to reducing I_{c0} .

PSLs explain some of the previously unexplained local features observed in TESs. As we will see in the next section, the phase-slip model is also strikingly successful at explaining much of the large-scale structure in $R(I, T)$ of TESs including reasonable predictions of α_I and β_I . The biggest drawback of the existing PSL model is that it does not take into consideration the exact geometry of typical TESs, i.e. noise mitigating bars and higher T_c leads. To predict the exact

position and density of the changes in n_{ps} in actual devices, it will likely be necessary to utilize the time-dependent G–L equations, which have been used successfully to model phase-slip behavior [143].

5.3. Comparing the resistance models

The previous sections described the major strengths and weaknesses of the new resistance models. Ultimately the true measure of the models is how well they predict the behavior of a given TES. The assertion made in the previous sections was that the weak-link model seems to describe much of the observed behavior of smaller devices, especially the behavior of the critical current with temperature and magnetic field. However larger devices and materials with smaller coherence lengths seem to not show the features of the weak-link model and instead are more consistent with the two-fluid and phase-slip models. In this section, we attempt to understand the regions of applicability of these models by looking at some of their more straightforward predictions: the dependence of critical current on temperature and β_I as a function of bias point. Later we will briefly compare the steady state response and predictions for α_I and β_I for the same or similar parameters and discuss how these models could be used to try to understand TESs.

5.3.1. Comparing predictions of $I_c(T)$ to measurements. It is clear from the models that α_I is strongly dependent on the logarithmic derivative of I_c with respect to T , i.e. equations (15) and (18) in the weak-link model, and equation (37) for the two-fluid. Also, as outlined in the previous sections, the physics that predicts different resistance models also predicts different forms for $I_c(T)$. In 2010, the $I_c(T)$ measured by Sadleir *et al* [110] was shown to be consistent with equation (8) for Mo–Au TESs with Mo/Nb leads up to $290\ \mu\text{m}$ long. However, for the larger devices, equation (8) appears to only be consistent with the data at very low I_c values very close to T_c . For example, for the $290\ \mu\text{m}$ TES, the fits are only consistent with the data within $0.1\ \text{mK}$ of T_c . Depending on the value of G for a given TES, biased devices can operate up to a few mK from T_c . This highlights the importance of understanding the range of

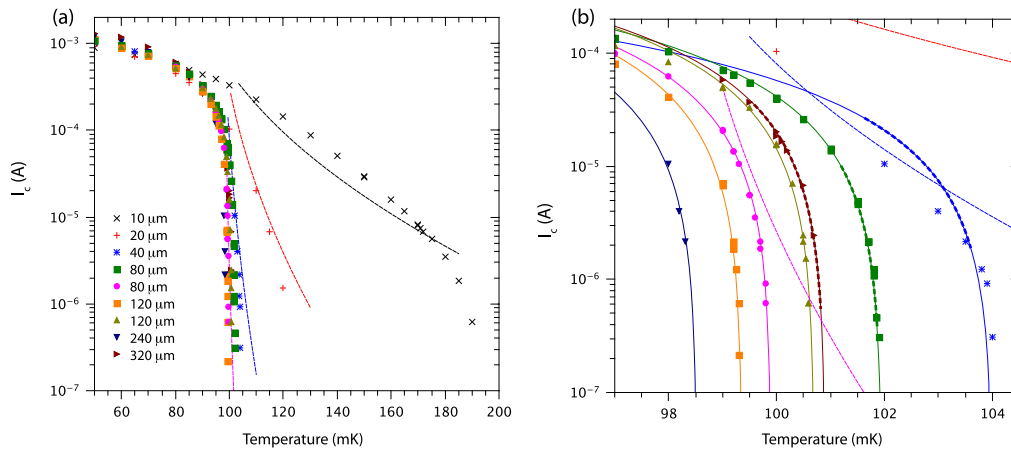


Figure 12. (a) Measured I_c as a function of temperature for a range of Mo–Cu TES sizes from 10 μm to 320 μm . The dashed lines are fits to the data of the same color using equation (26) with $\xi_N = 230$ nm. All the TESs were fabricated simultaneously on the same chip. (b) The same data and fits as (a) but scaled to show the region around T_c for the larger devices. The additional solid lines in (b) are fits to equation (33). The thicker dashed regions around some of these fits represent the typical temperature range during operation.

temperatures in which the device is being operated when choosing an appropriate $I_c(T)$ for a given model.

Figure 12(a) shows a recent measurement of $I_c(T)$ for Mo–Cu TESs with Mo leads for square TESs from 10 to 320 μm . There are three differences between the TESs in figure 12(a) and those measured in [110]. First, the bilayer material is Mo–Cu rather than Mo–Au. There is no reason to believe that this should have a significant effect on $I_c(T)$. Second, the leads are made of Mo rather than a Mo/Nb bilayer which should decrease ξ by approximately a factor of two (the square root of the ratio of the two material's T_{cL}). Finally, in order to avoid Mo shorts and to compare to device designs typically used for spectroscopy, these devices have Cu banks along the edges of the device. The effects of similar banks have been described using a lateral inverse proximity effect [111]. The banks can reduce the critical current by changing the effective size of the device and have been shown to reduce the visibility of the lobes of the weak-link interference pattern in $I_c(B)$.

For the smallest TESs (10 and 20 μm), the $I_c(T)$ is consistent with the weak-link model above the intrinsic T_c of the Mo–Cu film. Fits to the smallest devices using equation (26) give a $\xi_N = 230$ nm. This is consistent with a slightly higher intrinsic coherence than is used to fit the data in Sadleir *et al* [110]. However, as the devices get bigger, a weak-link interpretation is inconsistent with the data. This is more clear in figure 12(b) which shows an expanded region of figure 12(a) around 100 mK. The solid lines are fits to equation (33) which should be appropriate for a two-dimensional thin film close to T_c .

For a subset of the devices, 40, 80 and 320 μm , the typical internal operating temperatures for a bath temperature of 80 mK are indicated by the thicker dashed lines overlapping the solid lines corresponding to the approximate temperature range for the device between 20% R_n and 80% R_n . The temperature range was calculated by using measured IVs at different bath temperatures to determine the power law dependence of the heat transport and then finding the

temperature that balances the measured electrical power created by the resistance and the measured thermal power removed by the thermal conductance. These ranges are specific to the thermal conductance of a given device at a fixed bath temperature, but are typical of the parameters where the best performance is achieved.

Over the range of operation of these TESs, for the TES with lengths 80 μm and larger, the measured values of I_c are consistent with equation (33). For the TESs below 80 μm , there is a crossover from I_c behavior consistent with weak-link effects to I_c behavior consistent with equation (33). It is likely that in this cross-over region, solution of the Usadel equations is necessary to predict $I_c(T)$ [145]. This implies a simple test of whether, for a TES biased in the transition, it is appropriate to use the weak-link model or some other model. If in the operating range of the biased device, equation (33) fits the data then the device is too long to exhibit weak-link behavior at this temperature.

5.3.2. Comparison of model predictions for β_I to measurements. It was indicated previously that α_I depends strongly on the details of $I_c(T)$. However, the predictions of the resistance models for β_I are independent of $I_c(T)$. Therefore β_I is a good parameter to compare different models and to try to evaluate the difference between different classes of devices. Figure 13 shows an updated and expanded version of figure 4 from Bennett *et al* [116].

The red region between equations (16) and (19) spans the possible range of β_I for equation (12) as a function of TES bias. The β_I predicted by the two-fluid model and the stable regions of the PSL model fall into the blue region bound by equation (19) on the high side. The points represent a wide variety of data from a number of different types of TESs. The open symbols are from NIST Mo–Cu devices while the closed symbols are a sampling of published data from other groups.

Roughly, the smaller devices with fewer normal-metal bars have the highest measured values of β_I . At values above

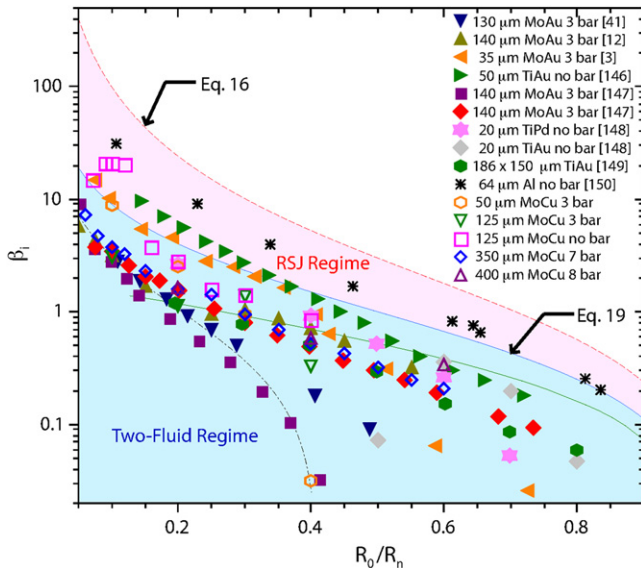


Figure 13. Measured values of β_I as a function of $\% R_n$ for a variety of TESs of different sizes and materials and different numbers of noise mitigating normal-metal features. The solid symbols are from the literature [3, 12, 41, 146–150] and the open symbols are measurements by our group. The red region is the range of β_I values predicted by equation (12) bounded on the high side by equation (16) (red dashed line) and on the low side by equation (19) (blue solid line). The blue region below equation (19) corresponds to the range of values of β_I predicted by the two-fluid and PSL models. The green solid line and black dashed-dotted line are representative examples of the PSL and two-fluid models respectively for a set of typical parameters. Reprinted figure with permission from [116]. Copyright 2013 by the American Physical Society.

50% R_n , all the measurements fall below equation (19) except the 64 μm aluminum TES bolometers with no normal metal bars [150]. In fact, the highest β_I across all bias points is achieved by these devices. Aluminum is known to have an especially long characteristic coherence length $\xi_0 = 1.6 \mu\text{m}$. Since these devices have Nb leads there is an additional boost in effective coherence length by a factor of almost 3. Therefore, it is not surprising that these aluminum TESs have β_I values consistent with the RSJ model.

For comparison, a prediction of β_I by the two-fluid model with $c_R = 0.41$ is shown by the black dashed line. A typical prediction of the PSL model assuming $c_I = 0.4$, $\Lambda_Q^* = 1 \mu\text{m}$ and $L = 350 \mu\text{m}$ is shown by the green solid line. Neither prediction is consistent with all of the data, but they do predict the correct order of magnitude for the β_I of many of the TESs and are roughly consistent with the overall trend of many of the devices.

5.3.3. Inter-model comparison. Given the models described previously, it is instructive to try comparing the predictions for a common set of device parameters. The parameters for the following calculations are based on measured values for the NIST Mo–Cu TESs presented in Swetz *et al* [10]. The superconducting film, $T_c = 121 \text{ mK}$, is $350 \mu\text{m} \times 350 \mu\text{m}$ square with 7 noise mitigating Cu bars that are $300 \mu\text{m}$ long

by $16 \mu\text{m}$ wide. The TES has a normal resistance of $10.4 \text{ m}\Omega$ and is in parallel with a shunt resistance of $337 \mu\Omega$. The power across the thermal conductance is given by equation (3) with $n = 3.4$ and $k = 450 \text{ nW/K}^n$. $T_b = 80 \text{ mK}$ unless otherwise stated. These devices are targeted for high resolution x-ray spectroscopy in the regime from 0.5 to 10 keV. Most of the parameters are very similar to other TESs optimized for the 6 keV x-ray range, i.e. the NASA Goddard MoAu TESs [41].

In order to compare the models, we must also choose a set of parameters specific to each model. An attempt was made to choose the parameters based on data or to scale parameters in a way that different regimes can be compared. This comparison is designed to highlight the general trends of the models and not to fit any specific data. When using equation (33), we will use the measured values for fits $I_c(T)$ that gives $I_{c0} = 20 \text{ mA}$. When using equation (8) for the weak link model we will arbitrarily use the same I_c and scale T_c down to 118.5 mK and $L/\xi^* = 70$ so that the two different definitions of temperature dependence have approximately the same IV dependence. For the two-fluid model, c_R is fixed to one so that there is no discontinuity in the transition. For the PSL model, the value of Λ_Q^* does not affect the large-scale structure of the transition and was therefore set at $1 \mu\text{m}$ so that the small scale features, a.k.a. jumps and wiggles, are suppressed on the scale of our comparison. For the PSL model, c_I is chosen to be 0.8. This appears to be a reasonable choice since previous measurements of this parameter for different materials fall in the range from 0.5 to 1.

At equilibrium, the Joule heating plus any external applied power equals the power that is removed through the thermal conductance G . Assuming the previously stated power law dependence and no externally applied power, this occurs when

$$I^2 R(I, T) = k(T^n - T_b^n), \quad (43)$$

where n is the exponent of the temperature dependence, usually between 3 and 4 for SiN_x , and k is a constant that satisfies $G = nkT^{n-1}$.

The calculated IV for the three different models is shown in figure 14(a). The weak-link IVs based on equation (14) and equation (17) are shown as red and magenta lines. The two-fluid model for $c_I = 0.8$ and $c_I = 1$ are given by the green and cyan line respectively. Finally the PSL model is given by the blue line. Despite the differences in the critical current dependence and the resistance mechanism, all the IVs look very similar. This is mostly due to the dominance of the thermal conductance in the shape of the IV.

It is easier to see the difference in the models when instead the TES power ($I \times V$) is plotted versus TES voltage as shown in figure 14(b). However all the models still look fairly similar, in part due to the scaling of the parameters for the comparison. The kink in the cross-over from the transition to the normal state that is observed in the two-fluid and PSL model is caused by the more abrupt temperature dependence of equation (33) as it approaches I_c . This sharp feature is likely rounded out in actual devices due to the proximitization

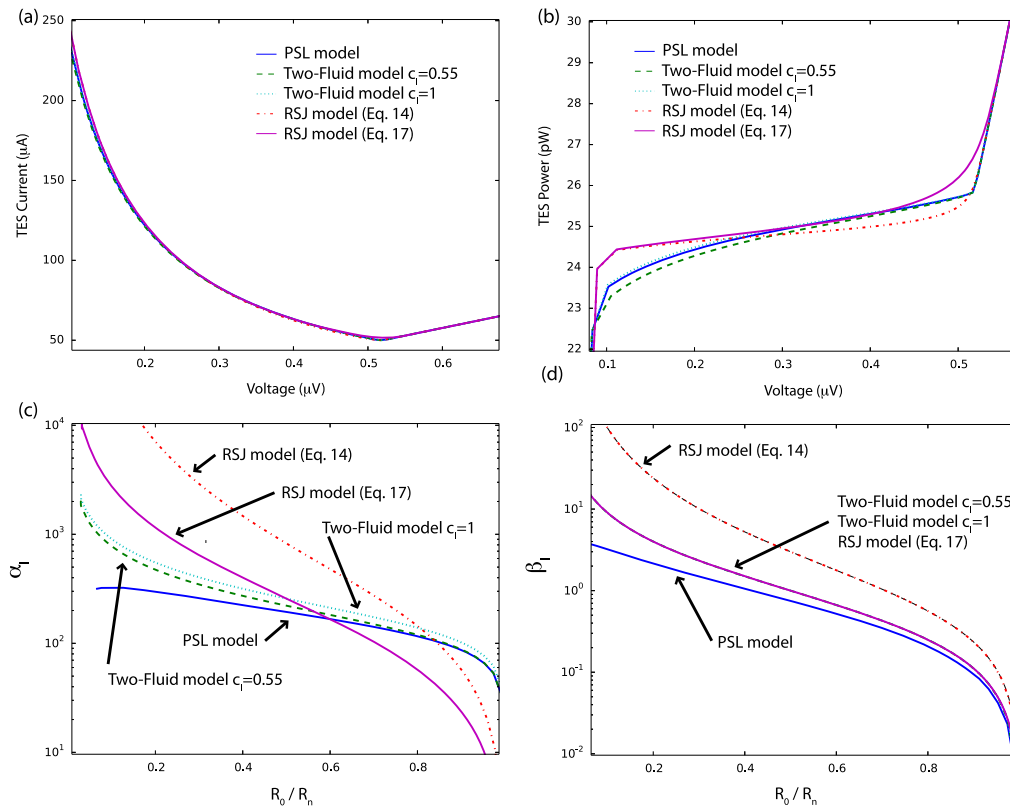


Figure 14. Comparing the different resistance models using (a) the current–voltage characteristic, (b) IV power versus TES voltage, (c) α_I versus $\% R_n$ and (d) β_I versus $\% R_n$. The models in the comparison are the weak-link model using equation (14) (red), weak-link model using equation (17) (magenta), two-fluid model using equation (36) with a $c_I = 0.55$ (green), two-fluid model using equation (36) with a $c_I = 1$ (cyan) and PSL model using equation (42) (blue). The weak-link models use the temperature dependence given by equation (8) and the other models use equation (33).

of the film by the leads. In fact most of the shape of the equilibrium curves is caused by the choice of $I_c(T)$. This is clearest in the difference between the model based on equation (17) (magenta solid line) and the two-fluid model ($c_R = 1$) (cyan dotted line) where the models are identical except for $I_c(T)$.

The difference between the resistance models is much clearer in the parameters that are directly related to the shape of the $R(I, T)$ surface, α_I and β_I . The simple models have analytic expression for α_I and β_I as was described in the previous sections [116]. α_I and β_I can be calculated numerically in any of the models but care must be taken to ensure that the α_I is calculated at constant current and β_I is calculated at constant temperature. Figure 14(d) shows the calculated β_I as a function of bias point at equilibrium for all the models. As was described in the previous section, the calculated β_I for the weak-link model based on equation (14) is exactly equation (12) and since $c_R = 1$ for the two fluid model, all the other models except for the PSL model fall exactly on top of each other as described by equation (16). For α_I , figure 14(c), the effect of $I_c(T)$ complicates the situation. In general equation (8) gives larger α_I lower in the transition and smaller α_I higher in the transition compared to equation (33). This is most clearly observed for the weak-link model based on equation (17) (magenta line) and the two-fluid with $c_I = 1$ model (cyan dotted line) where the

functional form of resistance is the same and only differ by choice of $I_c(T)$.

The largest problems with comparing the models to measured α_I and β_I has been the inability to match across the whole transition, i.e. in the two-fluid model [118], and the over prediction of the values, i.e. by a factor of 10 in the weak-link model [119]. The PSL model seems to do a better job predicting the overall trends of α_I and β_I , especially in larger TESs. More data and careful comparisons will be necessary to fully understand the strengths and weakness of these models and how they will need to be improved. However their full description of the transition can be helpful in optimizing TES operation and, as the next section will show, can be applied to modeling in the large signal limit.

5.4. Large-signal limit

The models discussed previously give a description of the resistance of a TES as a function of temperature, current, and field and therefore allow the evaluation of α_I and β_I at all points in the transition. If the resistance is known at all points in the transition, then one can begin to model TESs in the large-signal-limit. There are a number of interesting applications of large-signal-limit models of TESs. One critical aspect of these models is that they can be used to predict the dynamic range of a given device. The dynamic range is a

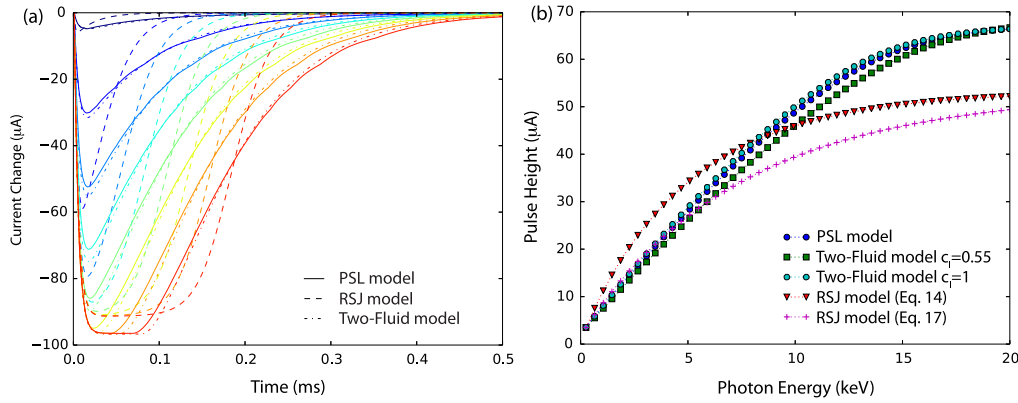


Figure 15. Simulated x-ray pulses in the large signal limit for different energies from 250 eV (dark blue) to 30 keV (dark red) for three different resistance models, PSL (solid), two-fluid (dashed-dotted), and RSJ (dashed). equation (33) was used for the PSL and TF models and equation (8) was used for the weak link model. (b) Calculated pulse height as a function of photon energy for the various models.

critical parameter for device design due to its close connection to achievable energy resolution. Large signal limit models can also be used to inform the energy calibration process by providing a theoretical basis for the calibration curves. Finally, the large signal limits models provide a mechanism against which we can fit pulses in order to better characterize existing devices and understand their optimization.

To calculate the large-signal limit behavior, we solve the standard nonlinear differential equations for the response of a TES, equations (1) and (2). Then one of the various resistance models is used for R_{TES} . Given initial conditions, the response of the TES at any time can be simply solved numerically. One of these models, the two-fluid model with $c_R = 1$, has been used previously to numerically model TESs in the large-signal limit [151]. Figure 15(a) shows simulated pulses for three different models for R_{TES} : phase-slip model (solid), two-fluid model with $c_R = 1$ (dashed-dotted), and weak-link model based on equation (14) (dashed). The energy range of the pulses runs from 250 eV (dark blue) to 20 keV (dark red). The bias voltage is chosen such that the equilibrium is 20% R_n . The equilibrium current is subtracted and the current is plotted as the change in current from the equilibrium value.

For the zero temperature RSJ model and the two-fluid model, β_I is only a function of bias point. At 20% R_n and in equilibrium, $\beta_I = 24$ and $\beta_I = 4$ for the zero temperature RSJ and the $c_R = 1$ two-fluid models respectively. Numerical calculation of the PSL model finds $\beta_I = 1.15$. The values of α_I are strongly dependent on the choice of model for the critical current dependence. Once again, the G-L temperature dependence (equation (33)) was used for the phase-slip and two-fluid models. Equation (8) was used for the weak-link model. The definition of I_{c0} is different in these two models. This difference, along with the different notions of T_c , makes it hard to compare the large signal limit models directly. At equilibrium, for the parameters and $I_c(T)$ used in figure 15(a), $\alpha_I = 4000$, $\alpha_I = 142$, and $\alpha_I = 222$ for the weak link model, two-fluid model, and PSL model respectively.

Figure 15(b) shows the pulse height as a function of energy for many more photon energies. Similar plots can be constructed for any of the typical analysis parameters of

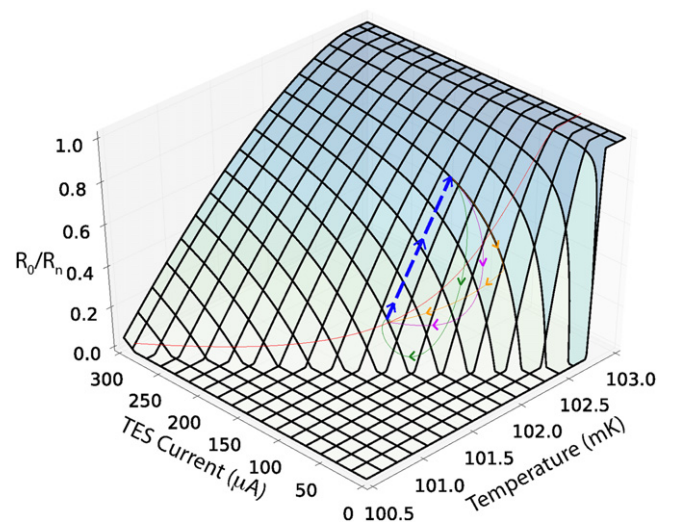


Figure 16. A surface plot of the resistance for the two-fluid model as a function of current and temperature ($R(I, T)$) for the parameters used in the previous figures. The red line shows the equilibrium values across the transition. The other lines are the trajectories of a 15 keV photon, assuming the photon is thermalized on times scales much faster than the detector response, for three different inductances, $L = 5$ nH (orange line), $L = 240$ nH (magenta line), and $L = 1$ µH (green line). The blue dashed line represents the initial response to the photon being rapidly thermalized on time scales faster than the TES current can respond.

interest, i.e. pulse area and optimally filtered pulse height. Efforts are currently in progress to compare the large signal limit predictions of the various models to data. If good agreement can be achieved, it opens up the possibility of using model-based design of TESs to optimize both energy resolution and dynamic range.

The dynamics of the pulse behavior are most easily visualized by viewing a pulse trajectory on top of the $R(I, T)$ surface. This is shown in figure 16 for the two-fluid model with $c_I = 0.55$. The surface shows the calculated resistance over a broad range of temperatures and currents. The red line gives the calculated resistance across the possible range of bias and gives the trajectory traced out by a dc IV curve. Pulse trajectories on the $R(I, T)$ surface are shown for a photon

energy of 15 keV and three different inductances; severely over-damped at $L = 5$ nH (orange line), under-damped at $L = 1$ μ H (green line), and close to critical damping at $L = 240$ nH (magenta line). The blue dashed line represents the very rapid temperature change when the photon is converted into heat. The thermalization happens on time scales much faster than the TES current can respond. When the pulse trajectory is viewed on the surface, it is clear how the pulses end up with slightly different shapes for different energies due to the differences in the local slope of the $R(I, T)$ surface. It is also clear how much α_I and β_I can vary during a pulse that is well into the large-signal limit.

5.5. Conclusion TES physics

The major advances in the last decade in the theoretical framework of TESs have been the new models put forth to describe the resistive transition of the TES. In order for TESs to become a mature detector technology, all aspects of the design and operation should be understood. The new models have the potential to fill the last remaining large hole in our understanding of TESs. Much work still remains to develop these theories and early models into mature and robust models that accurately describe the many varieties of TESs that are in use in many different instruments. The next important steps are models that take into consideration the specific materials and geometries of individual devices. A number of groups worldwide are actively involved in the detailed measurements necessary to thoroughly test these new ideas. We should expect many more advances in our understanding of TESs in the next ten years.

6. Applications

In the following section, we describe a series of measurement applications for superconducting x-ray and gamma-ray spectrometers. Having motivated the technology, we follow with a short description of key instrumental parameters.

6.1. Nuclear materials analysis using x-ray and gamma-ray spectroscopy

The non-destructive analysis (NDA) of nuclear materials is important to the nuclear fuel cycle and to global security because of the need for proper management and accounting of radioactive and, especially, fissile material. The state-of-the-art tool for photon-based NDA is the high-purity germanium (HPGe) sensor which is used to perform spectroscopy of hard x-rays and gamma-rays. Different radioactive elements and isotopes emit photons with identifying energies. A wide range of other sensors exist for the detection of particles and photons but HPGe is preferred for high resolution hard x-ray and gamma-ray spectroscopy. The spectral resolution of HPGe sensors is determined by the statistics of charge creation and collection and is limited to about 400 eV FWHM at 100 keV. While this performance is excellent, it is not sufficient to resolve a number of overlapping spectral lines from elements

relevant to the nuclear fuel cycle. These spectral overlaps have motivated the development and application of superconducting sensors to nuclear materials analysis. The brightest spectral lines of interest fall between about 40 and 200 keV. This is also the most complex spectral region with many closely spaced lines. Photons in this range can be observed from actinide-bearing samples with minimal shielding; heavily shielded material is typically analyzed using spectral features at higher energies. Even at 40 keV, it is challenging to absorb photons in a thin film. The need for useful detection efficiencies has catalyzed the development of two-body sensors in which a bulk absorber is attached to a much smaller thermometer. For gamma-ray detection, early success was achieved with semiconducting thermistors and superconducting tin absorbers [15] and tin absorbers subsequently worked well with TES thermometers [152]. The degradation of calorimeter energy resolution with increased heat capacity has so far limited the area of individual calorimeters designed for the 40-200 keV range to a few mm^2 . Since the collecting area of a HPGe sensor is at least several cm^2 , achieving comparable collection efficiency requires the use of arrays of superconducting sensors. Early steps were made with frequency-domain multiplexing [68] and more recent work has focused on time-domain and microwave SQUID multiplexing [44, 87]. At the present time, a 256 sensor spectrometer developed by NIST is in use at Los Alamos National Laboratory (LANL). This instrument relies on time-domain multiplexing with 32 pixels per readout column. While energy resolution values as good as 22 eV FWHM at 97 keV have been demonstrated [153] in single TES calorimeters, the full NIST/LANL spectrometer has shown 53 eV FWHM resolution at 97 keV using somewhat larger pixels. A description of the instrument is given in [40].

The resolution values achievable with superconducting sensors are sufficient to resolve almost all spectral line overlaps of interest. For example, as shown in the plot figure 17 from [154], the gamma-ray emission from fissile ^{235}U can readily be distinguished from that of ^{226}Ra , an isotope found in common commercial products including cat litter and roofing tiles [155]. Confusion between these two isotopes is a source of false alarms at U.S. border crossings [156]. However, proof-of-principle measurements such as figure 17 and others [157] do not immediately translate into practical application. The cost and complexity of superconducting spectrometers remain obstacles to their penetration into challenging field environments. In the near term, a more accessible but also more complex application is the quantitative measurement of isotopic fractions in complex actinide measurements. Measurements of this type are routinely performed for materials accounting purposes in large facilities related to the nuclear fuel cycle. Here, a small number of spectrometers operating in analytical laboratories could have a significant practical impact.

NDA performed with HPGe sensors can determine isotopic mass ratios with relative errors as good as 1% meaning, for example, a measurement showing that the mass ratio $^{240}\text{Pu}/^{239}\text{Pu}$ is 5.00 \pm 0.05%. Measurements of isotopic ratios used in combination with total activity measurements based

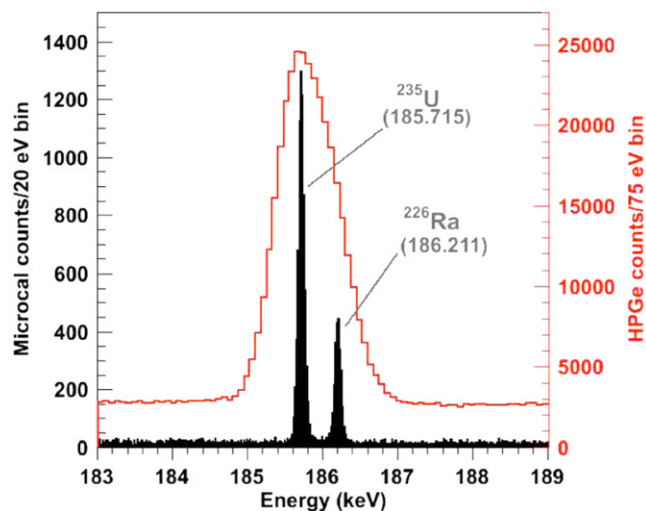


Figure 17. Measurement of the ^{235}U 185.715 keV gamma-ray line and the interfering ^{226}Ra 186.211 keV line. Results are shown from a HPGe detector (red) and a TES array (filled black). The two gamma-ray peaks are easily separated by the latter. The isotope ^{235}U is used in nuclear weapons while ^{226}Ra is found in commercial products including cat litter and roofing tiles. Confusion between the two isotopes is undesirable. Reprinted with permission from [154].

on neutron counting or conventional total power calorimetry provide absolute isotopic masses (kg) in a sample. In facilities with large mass throughput such as fuel reprocessing centers, 1% errors produce substantial uncertainties in the total mass budget of material handled at the facility. Destructive analysis (DA) techniques based on mass spectrometry can determine isotopic fractions to much better levels than NDA but DA techniques are more challenging, require extensive sample handling, consume the sample under study, and generate radioactive waste. A key challenge for superconducting detectors is to reduce NDA errors below 1% and towards the levels possible with DA. In addition, more precise knowledge of isotopic fractions can help constrain the age, origin, and intended purpose of material. For example, the ratio of Pu isotopes in a sample depend on the type of reactor where the sample was manufactured and on whether the reactor was operated for electricity or weapons production.

A series of measurements at Los Alamos National Laboratory conducted using the NIST-constructed spectrometer described above have contributed to a significantly better understanding of the NDA challenge. There are several aspects to this complicated problem. The first is the need for high statistics. For 1% relative errors, individual x-ray and gamma-ray lines of interest must contain at least 10^4 counts. This statistical threshold was crossed in Jethava *et al* [158] and has since become routine. As shown in figure 18, useful Pu spectra will contain 10^7 – 10^8 or more counts distributed among many bright spectral lines as well as an unavoidable continuum due to, at a minimum, Compton scattering in the source and in the detectors. For a 256 sensor array counting at 10 cps per sensor, a 10^8 count spectrum requires close to 11 hours of integration time. Whether integration times of this length are acceptable depends on the measurement scenario,

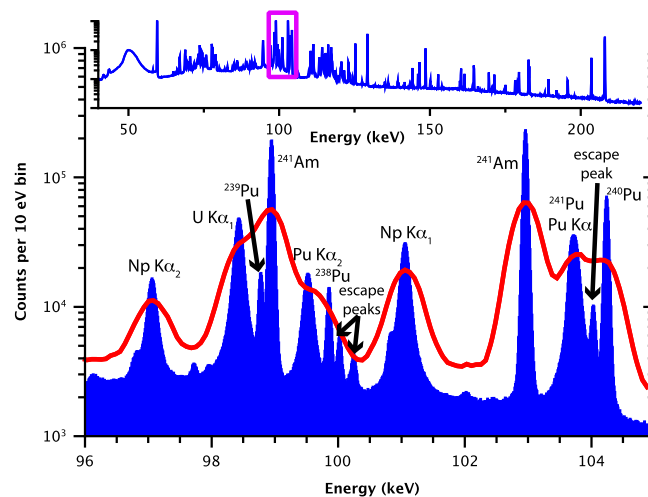


Figure 18. At top, TES x-ray and gamma-ray spectrum from a mixture of Pu isotopes and other actinides. The spectrum spans the energy range 40–220 keV and contains both bright spectral lines and a broad continuum. Quantitative determination of isotopic ratios from such spectra is a cornerstone of non-destructive nuclear materials analysis. At bottom, zoomed view of the 96–105 keV region. Results from a HPGe sensor are shown in red and those from a TES array in blue. The TES array easily resolves the closely spaced, isotope-specific peaks. Reprinted with permission from [40]. Copyright 2012, AIP Publishing LLC.

but in comparison HPGe sensors can count at up to 40 kcps without significant energy resolution degradation [159]. Hence, faster superconducting spectrometers remain desirable for the measurement of intense sources and more efficient superconducting spectrometers remain desirable for photon-starved cases.

A second component of NDA is turning knowledge of peak areas into knowledge of isotopic fractions. This conversion depends on parameters of nature such as branching ratios, half-lives, line energies, and mass attenuation coefficients, as well as details of the experiment such as the effective efficiency curve from self-absorption in the source and absorption by the detector. A triumph of gamma-ray NDA is the development of software tools for HPGe to extract the effective efficiency curve from a spectrum under analysis without other, outside information [160]. The effective efficiency curve allows isotopic activity ratios to be deduced from spectral peaks at different energies. Then, activity ratios can be converted to mass ratios using tabulated half-life and branching fraction data. A modernized version of this software has been developed for superconducting sensors [161] and applied in a series of measurements on different actinide mixtures. The measurements have shown that the statistical errors in microcalorimeter measurements of isotopic ratios are reduced compared to HPGe results for comparable numbers of counts. For some isotopic ratios, the reduction in statistical error is a factor of 3–5 although lower factors are more common [161, 162].

Final determination of isotopic ratios in complex Pu mixtures and comparison to results obtained using DA techniques must also include systematic errors. Uncertainties in

tabulated parameters of nature can introduce important relative errors into isotopic mass ratios. For both HPGe and superconducting sensors, uncertainties in branching fractions introduce relative errors near 1% into many isotopic ratios. However, the performance of superconducting sensors provides greater robustness to some sources of systematic error, in particular uncertainties in line energies. Because spectral peaks are so well resolved in microcalorimeter data, line centroids can be treated as free parameters without introducing large statistical errors in peak intensities. In contrast, line overlaps in HPGe data make it desirable to fix certain peak centroids at their expected energies to limit statistical error at the expense of increased systematic error. For HPGe, uncertainties in line energies can introduce relative errors in isotopic ratios as large as 6.9% depending on the sample, the isotopes, and certain analysis assumptions [162]. In contrast, the error contributed to microcalorimeter results from line energy uncertainties is almost negligible. While these early results are promising, more data on more samples and also improved data are needed to fully understand and demonstrate the capabilities of superconducting spectrometers for nuclear materials analysis. For example, the shape of well-isolated spectral lines in microcalorimeter data conforms less well to simple spectral models than does data from HPGe, presumably due to temporal gain variation. This effect is magnified if the spectra from many individual pixels with different resolution values are co-added prior to the calculation of isotopic ratios. While not fundamental, such effects presently complicate spectral analysis of microcalorimeter data.

At this time, it is unclear whether superconducting sensors will enable a large improvement in NDA capabilities although such improvements are predicted by work to date. The 40 year development history of HPGe has afforded ample opportunity to refine HPGe NDA analysis using measurements of large sample sets whose composition was known from DA. Similar work remains to be attempted for superconducting sensors. Direct improvements in tabulated branching fraction data could further enhance the value of microcalorimeter measurements. The current situation should be taken as strong motivation for further work in this very important application area.

While the chief obstacles to demonstrating the analytical value of superconducting sensors for gamma-ray NDA are presently related to spectral interpretation, improvements in spectrometer performance will also be valuable. As noted above, higher system count rates are needed to match HPGe measurements. In addition, the absorption efficiency of superconducting sensors lags HPGe. While the spectrometer of Bennett *et al* [40] and a high-quality planar HPGe sensor both have active areas of 5 cm^2 , a typical Ge crystal is at least 1 cm thick, in contrast to the $385 \mu\text{m}$ thick Sn absorbers used in [40]. Absorbers with higher Z and lower specific heat than Sn are desirable. It is worth noting that spectrometers developed for hard x-ray and gamma-ray nuclear materials analysis could be used for other applications including Compton scattering [163] and gamma-ray astrophysics [15].

Nuclear materials decay via paths in addition to gamma-ray emission. These paths include neutron, alpha, and beta decay. Cryogenic sensors can perform high resolution spectroscopy of neutrons [164], alpha [165], and beta particles [166] as well as of total reaction energies [167, 168]. The measurement of reaction energies to determine material composition is related to the measurement of reaction energy for basic physics experiments such as searches for neutrinoless double beta decay [169] and direct measurements of the neutrino mass [76, 89, 170]. While there is considerable overlap between the sensor technologies used for these applications and the sensor arrays used for x-ray and gamma-ray spectroscopy, particle detection applications fall outside the scope of this article and are not discussed further.

6.2. Microbeam analysis

One of the original motivations for the development of superconducting x-ray detectors is the potential for materials analysis on scanning electron microscopes (SEMs) [171]. X-ray analyzers are already widely used on SEMs to identify materials from the x-ray fluorescence induced by the electron beam. This technique has applications ranging from the study of ceramics to criminal forensics. SDDs are presently the most common x-ray detector on SEMs. Superconducting sensors and SDDs have similar broad-band response and simple efficiency curves. However, the energy resolution of superconducting detectors is significantly better; SDDs achieve about 125 eV FWHM resolution at 6 keV and about 50 eV FWHM at 677 eV (fluorine $K\alpha$). Better energy resolution is helpful to resolve overlaps between fluorescence lines, particularly at energies below 2 keV. Small features and thin films must be analyzed at low beam voltages in order to localize the electrons to the material of interest as opposed to the substrate below. Low energy electrons can only excite low energy x-rays, so analysis of submicron structures often relies on features with x-ray energies below 2 keV. An energy resolution near 10 eV is sufficient to resolve most line overlaps. Technologically relevant examples of line overlaps include the detection of hafnium against background x-rays from Si. Hafnium oxides are used as high-k dielectrics in transistor gates. The M x-rays of Hf fall between 1.645 and 1.698 keV whereas the Si $K\alpha$ complex is centered on 1.740 keV. Tungsten is used in integrated circuits in a variety of interconnection roles. The M lines of W fall between 1.775 and 1.835 keV and are also challenging to detect against a Si background using conventional sensors. Other overlaps include Ti/N and Ta/Si. Fluorescence detection is not limited to qualitative analysis; quantitative composition measurements are possible in combination with either reference samples or models of x-ray generation and propagation [172, 173].

Even better resolution, near 2 eV or below, enables the detection of slight changes in x-ray line shapes and positions due to the bonding state of the target element. These spectral features are sometimes but not universally called chemical shifts. For example, the Al $K\alpha_{1,2}$ and $K\alpha_{3,4}$ peak energies are slightly increased in Al_2O_3 compared to metallic Al

[174–177]. While a significant challenge, the ability to routinely detect these small spectral changes would extend SEM x-ray analysis to chemical analysis which would be a dramatic increase in measurement scope. Presently, this level of chemical detail can be obtained using x-ray photoelectron spectroscopy (XPS) but XPS requires excellent vacuum conditions and is limited to surface analysis.

Coupling superconducting detectors to a SEM is a significant technical challenge. The safety and ease-of-use issues from liquid helium are nearly insurmountable outside of a cryogenic research laboratory while vibration levels from mechanical cryocoolers must be compatible with imaging at high magnifications. The superconducting spectrometer must closely approach the specimen beneath the pole piece of the microscope with little or no modifications to the specimen chamber. Sensor resolution and gain stability must be preserved during operation of the SEM which includes the use of large magnetic fields in the electron optics. Pulse data must be processed in real time with little user intervention and the spectrometer must be easily operated by non-experts. Despite these many challenges, important proofs-of-principle were conducted with an instrument at the NIST Boulder laboratories beginning in the 1990s [171]. These measurements included demonstrations of chemical shift detection [178, 179]. A commercial instrument called POLARIS from Vericold appeared in 2002 [180]. This instrument contained one TES x-ray sensor and a polycapillary optic to increase the effective solid angle of the sensor. Vericold was purchased by Oxford Instruments in 2007 and the POLARIS was discontinued. More recently, Star Cryoelectronics has brought the MICA-1600 system to market [181, 182]. This instrument contains an array of TES x-ray sensors for increased collection area and count rate. A ≈ 20 cm long cold finger at sub-100 mK temperatures approaches to within 4.5 cm of the specimen. The cold finger and its three radiation shields enter the specimen chamber through the existing spectroscopy port which has a diameter of only 3 cm. An image of the MICA-1600 and representative spectral data are shown in figure 19.

At time of writing, most of the technical challenges to the use of TES x-ray spectrometers on SEMs have been overcome. Whether use of the technology becomes widespread will depend heavily on the cost of future systems. One important remaining technical challenge is the routine detection of chemical shifts. If this level of performance can be achieved in commercial spectrometers, the attractiveness of these instruments will be significantly increased.

6.3. Beamline science

Modern x-ray science is increasingly performed at large facilities such as synchrotrons and free electron lasers because these facilities produce unmatched x-ray fluxes and often have other useful properties such as ultrashort pulses or nearly monochromatic beams. So, it is natural to ask if transition-edge detectors have a role at these facilities. The extreme fluxes at large x-ray facilities will overwhelm the count rate capability of present and probably future LTD arrays in applications that require measurement of the primary beam.



(b) Sample: W (20 nm) over Ta (20 nm) on Si

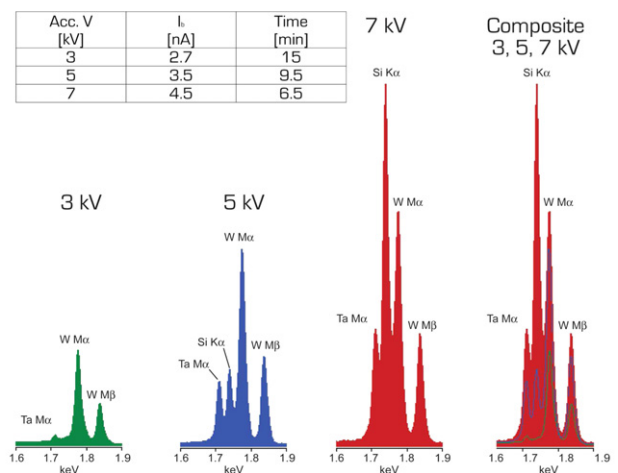


Figure 19. A commercial x-ray spectrometer based on an array of TES sensors is shown in (a) mounted to a scanning electron microscope. The spectrometer is on the left side of the image and a cold finger containing the sensors extends into the specimen chamber of the microscope at center. The spectrometer provides compositional data that complement morphological information from the electron beam image. X-ray spectra obtained on an electron microscope using TES detectors are shown in (b). Spectra are shown for electron beam accelerating voltages of 3, 5, and 7 kV. The specimen consists of thin tungsten and tantalum films on a silicon substrate. X-ray fluorescence lines from Ta, W, and Si are clearly resolved by the TES sensors. As the accelerating voltage is increased, electrons penetrate deeper into the sample and the fluorescence yield from the buried Ta layer and the silicon substrate increases. These spectra illustrate why thin structures must be probed using low beam voltages. In related work, fluorescence ratios have been correlated with film thicknesses [183]. Photograph and figure courtesy of Robin Cantor, STAR Cryoelectronics.

However, the situation is much more promising for so-called photon-in, photon-out measurements in which LTD sensors are used to detect x-rays produced by or scattered from the main beam. Examples include fluorescence detection similar to on a SEM and fluorescence-detected absorption spectroscopy. In the latter, x-ray fluorescence yield is measured as a monochromatic excitation beam is scanned in energy. Scanning over an elemental absorption edge provides a measurement of the unoccupied density of states of the element in question. Here, the energy resolution of the density of states

measurements is provided by the monochromatized exciting beam. However, the energy resolution of cryogenic sensors allows elemental x-rays excited by the primary beam to be unambiguously counted in the presence of x-rays from other elements and from the scattered excitation beam. Measurements of this type have been successfully performed with both STJs and TESs [184–186].

Another measurement of interest is emission spectroscopy which is a close cousin to fluorescence detection but that differs by requiring much higher resolving powers in order to extract more subtle information from the detected x-ray energies. In emission spectroscopy, the energy distribution of the detected x-rays from a single element at a single excitation energy is used to deduce the occupied density of states of that element which, in turn, is indicative of its chemical environment. Hence, emission spectroscopy at a large x-ray facility and chemical shift detection on a SEM differ primarily in the excitation mechanism. Emission spectroscopy at a synchrotron using TES arrays was first demonstrated to distinguish between two nitrogen-bearing explosive compounds. These data and a detailed analysis of the potential of TES arrays for emission spectroscopy at large facilities were presented in Uhlig *et al* [187]. The key arguments are (1) while the energy resolution of cryogenic sensors is unlikely to be as good as competing gratings and crystals, the resolution of cryogenic sensors can be comparable to the natural life-time broadening that sets the energy-scale of many spectral features of interest, and (2) the collection efficiency of arrays of superconducting x-ray sensors is potentially several orders of magnitude larger than competing gratings and crystals. Increased collection efficiency is desirable for a range of photon-starved experiments including measurements of dilute samples, radiation-sensitive samples, and time-resolved measurements.

A tremendous diversity of measurement techniques are employed at large x-ray facilities and describing this diversity exceeds the space available here. A few examples of additional opportunities for superconducting spectrometers include Compton scattering, energy-resolved diffraction, and resonant inelastic x-ray scattering where an emission spectrum is generated for each setting in an energy sweep of the exciting beam. Overall, the future of superconducting sensors at large x-ray facilities appears bright. Perhaps the largest outstanding challenge is to streamline and automate the pulse processing from the arrays of hundreds to thousands of sensors that are needed to obtain interesting collection areas and count rates.

6.4. X-ray astrophysics

X-ray astrophysics is one of the original motivations for the development of cryogenic microcalorimeters [188] and strong interest in this application continues to the present day. X-rays are emitted by ionized atoms and energetic electrons found near active objects such as black holes, supernovae remnants, and neutron stars. Both x-ray emission and absorption are interesting; the absorption of x-rays emitted from hot objects by intervening dust and gas is a useful probe of tenuous

material that is difficult to detect by other means. The energies of discrete x-ray lines reveal the constituent elements, and x-ray line energies and shapes can reveal kinematic conditions through Doppler effects. Highly ionized atomic species are common, resulting in great spectral complexity. The binding energies of electronic orbitals are altered by the degree of ionization so families of x-ray lines will be present for different ionization states of the same element. Further, there are multiple ways to populate the orbitals of an atom with a particular degree of ionization. The density and temperature of astrophysical plasmas can be determined from line ratios within these complex spectra [189].

Astrophysical x-rays are not accessible from the surface of the earth because of atmospheric attenuation; instead they are measured from sounding rockets and satellites. The scarcity and cost of measurement opportunities argue for the use of efficient detectors. Further, much of the spectral detail described above can only be probed by sensors with excellent resolving power. The recent satellites Chandra and XMM-Newton use gratings to perform high-resolution x-ray spectroscopy. Cryogenic microcalorimeters offer higher efficiency, higher resolving power at energies near 6 keV, and better performance for spatially extended sources. Small arrays of X-ray microcalorimeters based on semiconductor thermistors have been used on a sounding rocket and a series of satellites [190–192]. Several mission concepts have been developed that include a TES microcalorimeter spectrometer with a kilopixel-scale array. At this time, the European ATHENA satellite mission has just been approved and an array of several thousand x-ray TES sensors will be one of the two main instruments on the satellite [69]. Work is also ongoing to launch a 111 pixel array of TES sensors on a sounding rocket [193].

Astrophysically-relevant plasmas are produced in terrestrial facilities and cryogenic microcalorimeters are also well suited for these experiments. Electron-Beam Ion Traps (EBITs) are used to produce plasmas with considerable elemental and charge-state selectivity. X-ray spectrometers based on small arrays of cryogenic semiconductor thermistors have produced a wide range of scientific results at EBIT facilities [194, 195]. For example, one such instrument was used to develop and validate a model for soft x-ray emission from comets based on charge exchange between the solar wind and cometary gas [196]. A larger array of TES x-ray sensors is under development for use at the Lawrence Livermore EBIT [197].

6.5. Other applications

The scope of applications for TES x-ray and gamma-ray spectrometers is considerably broader than just the topical areas listed above. Any application that simultaneously requires high spectral resolving power and high collection efficiency is a good candidate for superconducting sensors. Some examples that are not readily categorized follow below. In proton induced x-ray emission (PIXE), protons are used to fluoresce x-rays from a sample under study. Suitable proton accelerators are intermediate in size between a SEM and a

synchrotron. Unlike exciting electrons, more massive protons do not produce a background of Bremsstrahlung x-rays thus lowering the detection limits for trace materials. Two groups have already combined PIXE analysis with TES sensors [198, 199].

Ultrashort pulse, near-infrared lasers are increasingly used to generate x-ray pulses in laboratory settings [200]. The motivation for these sources is to perform optical pump, x-ray probe measurements with time resolution approaching the pulse durations which can be picoseconds to attoseconds depending on the source design. X-ray pulses of such short duration are challenging to generate at synchrotrons where the characteristic electron bunch length is about 100 ps. X-ray free electron lasers are designed to produce pulses of 100 fs duration or less, but these facilities have only emerged in the last few years and beamtime is scarce. Hence, laboratory laser-driven x-ray sources may play an important role in studies of dynamic behavior such as the rearrangement of atoms during photoreactions. These novel x-ray sources are dim on an absolute scale so arrays of superconducting x-ray sensors may enable spectroscopic measurements such as time-resolved absorption and emission spectroscopy. The x-ray fluxes at large facilities are so high as to preclude using a superconducting spectrometer to measure the primary beam but fluxes from these laboratory sources are sufficiently low that x-ray absorption spectroscopy can be performed by a direct measurement of the x-rays transmitted through the sample of interest. A static measurement demonstrating this approach was recently performed where the energy resolution of the absorption spectrum was provided entirely by the sensors since the laser-drive source was intrinsically broadband [201].

Yet another emerging application is the measurement of x-rays from exotic atoms [202] in which an orbiting electron has been replaced by a particle such as a kaon or pion. Such atoms are produced at large accelerator facilities by bombarding a target with a kaon or pion beam. The absolute energy and energy width of the x-ray lines produced by transitions of the exotic particle between orbital levels reveals details of the nuclear and atomic physics in these unusual atoms.

The already wide range of applications for superconducting spectrometers described above strongly suggests that new applications will continue to emerge. One example that is suggested by the need for absolute energy measurements of the x-rays generated by exotic atoms is x-ray metrology. At energies below 10 keV, a small number of x-ray energies have been determined with milli-eV accuracy or better using diffraction measurements from material whose atomic spacing is known with great precision from coupled optical and x-ray interferometry [203]. However, the vast majority of x-ray transition energies carry much larger uncertainties. Can these transition energies be determined using superconducting spectrometers whose response curves are calibrated using the much smaller number of x-ray lines whose energies are already known with metrological accuracy? The fine details of the superconducting transition shape discussed in section 5 which determine the smoothness of a

sensor's gain curve will strongly affect the prospects for success of such a metrology effort. The simple, smooth efficiency curve of superconducting sensors suggests that measurements of parameters such as relative fluorescence yields among families of x-ray lines will be possible. A compilation of chemical shifts, while ambitious, would also be valuable. Our group at NIST is just beginning to explore these topics. An early experiment to determine the absolute energies of several lanthanide transition energies shows promise.

7. Instruments

Spectrometers based on TESs and other low temperature detectors involve considerably more components than just the TES array. Specialized cryostats are required that can reach the necessary operating temperatures, typically near 50 mK. Precooling to a temperature near 4 K is needed regardless of the scheme for reaching base temperature. The emergence of low-vibration pulse tube coolers that reach 4 K using a sealed charge of He gas [204] eliminated the need for liquid cryogenics and thereby played an important role in enabling spectrometers that can be operated outside of a cryogenics laboratory. To reach the milliKelvin regime, two-stage adiabatic demagnetization refrigerators (ADRs) [205] have proven attractive because they do not require a large external gas circulation system and because the modest heat load from arrays of cryogenic sensors is well matched to the capacity of this cooling technique. The use of more powerful but also larger dilution refrigerators may increase as array sizes grow and as the reliability of this cooling technique improves. Hybrid cooling architectures such as ADRs backed by sorption-pumped helium may also play a larger role in the future.

Almost all x-ray and gamma-ray sources of interest must reside outside the spectrometer intended for their measurement. Hence, a windowing scheme is needed that allows the photons of interest to travel from their 300 K source to the sub-Kelvin detectors while blocking infrared photons that would otherwise overwhelm the detectors or their associated cryogenics. Typically, a vacuum window is required along with multiple infrared blocking windows at successively colder stages of the cryostat. This windowing is easily accomplished except for x-rays with energies of a few keV or lower. For these low energies, specialized vacuum windows are required; fortunately, cooled semiconductor detectors have a similar need and suitable windows are available from a variety of vendors. For infrared (IR) blocking, thin (20–100 nm) films of aluminum combine good IR rejection with high x-ray transmission. These films are usually, but not always, deposited on a supporting layer of a low-Z material such as Lexan or polyimide. X-ray spectrometers developed at NIST use IR-blocking filters at the 50 mK, 3 K and 50 K stages of the cryostat. Typical window areas are 1 cm² or larger. Since the failure of any single window in a stack can compromise spectrometer performance, or even result in serious damage in the case of the vacuum window, considerable effort is often required to develop a robust windowing scheme that also provides very high transmission for low energy x-rays. Some

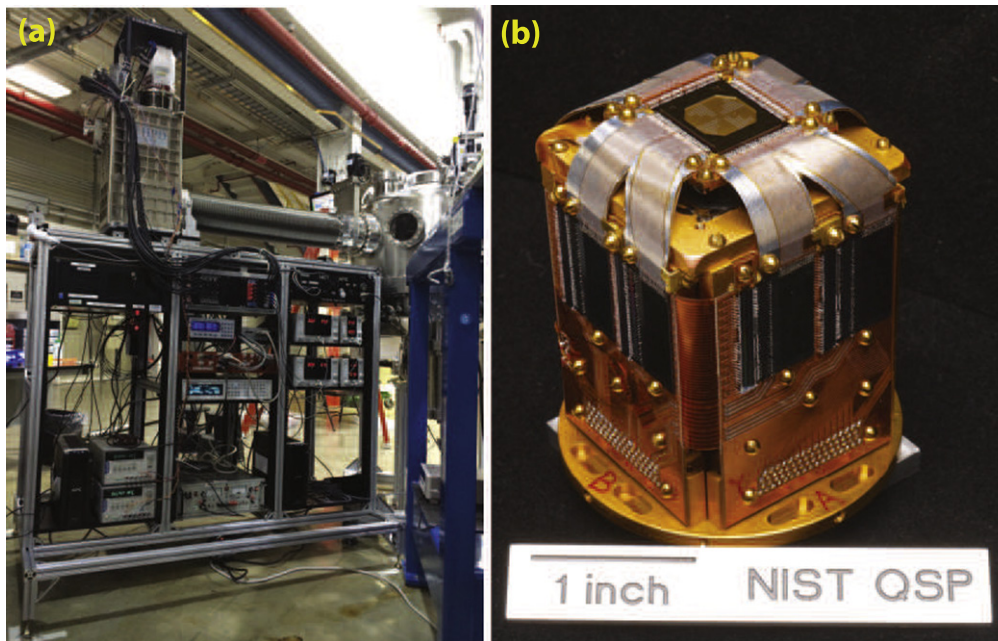


Figure 20. (a) Photograph of the complete NIST TES x-ray spectrometer installed at the Advanced Photon Source in Argonne, Illinois. The spectrometer is on the left and the synchrotron beamline is on the right. The snout of the spectrometer is contained in the central bellows and can be inserted into the beamline by shifting the spectrometer with a translation stage. The bellows contains the 300, 50, and 3 K shields of the snout as well as the milliKelvin detector package. Control electronics are located below the spectrometer. (b) Photograph of detector package incorporating 240 TES x-ray sensors and time-domain SQUID multiplexing circuitry. The detector array and a silicon collimator are at top. Multiplexer circuitry is located on the four sides of the package connected by superconducting flexible wiring. The package is cooled below 100 mK during operation.

design refinements to IR-blocking windows include integral heaters to drive off frozen moisture and micromachined supporting structures [190, 206, 207]. In addition, as shown in figure 20, it is often convenient for the detector package, its radiation shields, their IR windows, and the vacuum window to protrude from the body of the cryostat in order to better approach or interface with the source of the x-rays. This protruding assembly is sometimes called a snout and often requires a high level of cryogenic engineering.

Arrays of superconducting sensors are needed to achieve useful collecting areas and count rates. Having a dedicated amplifier per detector imposes strict limits on array size because of the mechanical complexity and thermal loading of the wiring, as well as the system expense. The recent emergence of TES spectrometers owes much to the development of multiplexing techniques that allow multiple detectors to be measured using a smaller number of amplifier chains. These techniques were summarized in section 3.

A spectrometer also requires hardware or software to turn electrical pulses at the top of the cryostat into energy-calibrated pulse heights. The difficulty of this task is particularly acute for arrays of cryogenic sensors. The same elevated resolving powers that make these detectors attractive also mean they are sensitive to small sources of noise and gain drift that can be ignored in other detector systems. Further, the complex shape of the superconducting transition means that the gain curves of individual TES sensors will likely never be similar to a level that is much smaller than the energy resolution of the devices. As a result, each sensor in an array will

require its own energy calibration before the output of different sensors can be coadded into a master spectrum. Pulse processing for TES arrays spans a range of topics including filter construction, techniques for addressing nonlinearity, techniques for addressing pileup, and the construction of accurate gain curves. There is active research in all of these topic areas. A brief summary was provided in section 4.

Work on TES sensors has been carried out at research laboratories around the world for more than twenty years. However, it is only in the last few years that complete x-ray and gamma-ray spectrometers based on TES arrays have emerged. Another characteristic of this development is that the purpose of these spectrometers is measurement science and not detector development. The first of these instruments was a 256 pixel hard x-ray and gamma-ray system at Los Alamos National Laboratory [40]. In addition, there are now x-ray spectrometers with 240 pixels at Brookhaven National Laboratory, Argonne National Laboratory, and the NIST Boulder Laboratories, and 160 pixel x-ray spectrometers at Lund University in Sweden and Jyväskylä University in Finland. These instruments were built by our group at NIST in collaboration with their intended users. So far, these spectrometers rely on time-domain SQUID multiplexing for readout and two-stage ADRs backed by pulse-tube coolers for refrigeration. In addition, STAR Cryoelectronics has supplied a growing number of spectrometers to industrial and scientific customers.

The spread of TES x-ray and gamma-ray spectrometers to new uses and new facilities will continue. Spectrometers

are presently under development for the EBIT at Lawrence Livermore National Laboratory [197] and at least one more x-ray light source. The ATHENA satellite program, if carried to completion, is likely to significantly advance the capability of TES instruments and result in spectrometers for astrophysics and other applications. The long-term prospects for x-ray and gamma-ray spectrometers based on superconducting sensors are also excellent. Some years from now, it would not be surprising to see these instruments in use at every large x-ray facility, at a wide range of laboratory x-ray sources, in laboratories for materials analysis, and in nuclear facilities for materials accounting.

8. Conclusion

We conclude with remarks on the use of TES sensors for x-ray and gamma-ray spectroscopy that span their current status and future prospects. These remarks reflect the personal perspectives of the authors; time will tell as to their accuracy.

- The energy resolution of single TES x-ray and gamma-ray sensors routinely approaches the predicted theoretical limits. Sensors can be fabricated for a particular energy range or application with a high probability of the results fulfilling the design goals. Future improvements in the energy resolution of single pixels will only be modest; the increased use of cryogenics that provide operating temperatures below 50 mK will contribute to resolution improvement.

- SQUID multiplexing techniques have already enabled TES spectrometers of up to 256 pixels. Time- and code-domain multiplexing are currently the most mature approaches. If sensor resolutions under AC-bias can consistently be achieved that match results under DC-bias, then the use of frequency-domain multiplexing will expand. All three techniques are compatible with arrays of several kilopixels.

- Presently, the energy resolution of multiplexed arrays is not as good as the best single pixel results. There is no fundamental reason for this degradation and the difference between single pixel and multiplexed performance will close as engineering improvements increase multiplexer bandwidth and reduce non-idealities such as cross-talk.

- Microwave readout techniques offer a path to TES arrays of 10^4 pixels or more. The combination of conventional and microwave readout techniques offers a path to still larger arrays. However, the effort required to develop such large detector packages and the necessary room temperature control electronics will be very significant.

- There is significant current activity to develop pulse processing techniques to address pulse pile-up and non-linearity and some promising results. Continued progress in this area will play an important role in the development of spectrometers for high count rate applications.

- Large arrays operating at high count rates pose significant data management challenges that will require innovative pulse processing solutions. For example, 10^3 sensors counting at 100 cps per sensor where each pulse record contains 500 14 bit samples will generate 700 Mbits s^{-1} of data.

- Two theories have recently been developed to describe the resistance surface in TESs: the shunted junction and PSL models. Growing evidence, including new results presented here, suggests that the resistance mechanism of individual TES devices falls on a continuum between the models depending on the ratio of the effective coherence length to the device length. This ratio is affected by the energy gap of the superconducting leads and the presence or absence of normal metal features. When the ratio is large, weak-link effects dominate; when it is small, devices are well described by a two-fluid model where PSLs provide a microscopic resistance mechanism. A single device can transition between the two models depending on the instantaneous current and resistance.

- Models for the resistance surface may provide useful guidance for pulse processing and energy calibration strategies that are valid in the nonlinear response regime. There is an opportunity for further work comparing model predictions for the shape of the resistance surface to data. There is also opportunity to expand models for the resistance surface so as to reflect the full geometric complexity of TES devices in routine use.

- Current performance levels appear sufficient or very nearly so to perform two the motivating applications for the original development of x-ray TESs: imaging spectroscopy on an x-ray satellite and materials analysis on SEMs. Tremendous progress has also been made towards realizing the goal of using TES gamma-ray detectors for nuclear materials analysis. Further improvements in spectrometer count rates and spectral stability will benefit all three applications and are particularly necessary for TESs to be accepted as tools for nuclear materials analysis.

- As the performance of TES x-ray and gamma-ray spectrometers improves, there is a virtuous circle where more applications become accessible, thus motivating further spectrometer development. The recent introduction of TES instruments to x-ray beamline science is a salient example of this process. We have briefly described some active applications and fully expect more to emerge.

Acknowledgments

We gratefully acknowledge support from the NIST Innovations in Measurement Science program, NASA, and the Department of Energy. The manuscript benefitted from discussions with numerous colleagues at NIST, Los Alamos National Laboratory, NASA, and elsewhere. Much of the work described in the manuscript was enabled by the efforts of current and former staff members in the NIST Quantum Sensors Project including Jim Beall, Dan Becker, Randy Doriese, Colin Fitzgerald, Joseph Fowler, John Gard, Jim Hays-Wehle, Gene Hilton, Rob Horansky, Kent Irwin, Young Il Joe, Vince Kotsubo, Peter Lowell, Ben Mates, Omid Noroozian, Galen O'Neil, Carl Reintsema, Daniel Swetz, Daniel Schmidt, Jens Uhlig, Leila Vale, and Barry Zink.

References

- [1] Enss C 2005 *Cryogenic Particle Detection* vol 99 (Berlin: Springer)
- [2] Mandl F 1988 *Statistical Physics* (New York: Wiley)
- [3] Smith S *et al* 2012 Small pitch transition-edge sensors with broadband high spectral resolution for solar physics *J. Low Temp. Phys.* **167** 168–75
- [4] Bandler S R *et al* 2013 Advances in small pixel tes-based x-ray microcalorimeter arrays for solar physics and astrophysics *IEEE Trans. Appl. Supercond.* **23** 2100705
- [5] Irwin K D 1995 An application of electrothermal feedback for high resolution cryogenic particle detection *Appl. Phys. Lett.* **66** 1998–2000
- [6] Moseley S H, Mather J C and McCammon D 1984 Thermal detectors as x-ray spectrometers *J. Appl. Phys.* **56** 1257–62
- [7] Lindeman M A 2000 *Microcalorimetry and the Transition-Edge Sensor* (Davis: University of California)
- [8] Irwin K D and Hilton G C 2005 Transition-edge sensors *Cryogenic Particle Detection (Topics in Applied Physics)* vol 99 (Berlin: Springer) pp 63–149
- [9] Ullom J N, Beall J A, Doriese W B, Duncan W D, Ferreira L, Hilton G C, Irwin K D, Reintsema C D and Vale L R 2005 Optimized transition-edge x-ray microcalorimeter with 2.4 eV energy resolution at 5.9 keV *Appl. Phys. Lett.* **87** 194103
- [10] Swetz D S, Bennett D A, Irwin K D, Schmidt D R and Ullom J N 2012 Current distribution and transition width in superconducting transition-edge sensors *Appl. Phys. Lett.* **101** 242603
- [11] Ullom J N, Doriese W B, Hilton G C, Beall J A, Deiker S, Duncan W D, Ferreira L, Irwin K D, Reintsema C D and Vale L R 2004 Characterization and reduction of unexplained noise in superconducting transition-edge sensors *Appl. Phys. Lett.* **84** 4206–8
- [12] Smith S *et al* 2008 Characterizing the superconducting-to-normal transition in Mo/Au transition-edge sensor bilayers *J. Low Temp. Phys.* **151** 195–200
- [13] Jethava N, Ullom J N, Irwin K D, Doriese W B, Beall J A, Hilton G C, Vale L R and Zink B 2009 Dependence of excess noise on the partial derivatives of resistance in superconducting transition edge sensors *13th Int. Workshop on Low Temperature Detectors-LTD13* vol 1185 (New York: AIP) pp 31–33
- [14] Porter F S *et al* 2010 The detector subsystem for the SXS instrument on the astro-H observatory *Proc. SPIE* **7732** 77323J
- [15] Eric H *et al* 2000 NTD germanium-based microcalorimeters for hard x-ray spectroscopy *Proc. SPIE* **4140** 397–401
- [16] Bandler S R, Irwin K D, Kelly D, Nagler P N, Porst J-P, Rotzinger H, Sadleir J E, Seidel G M, Smith S J and Stevenson T R 2012 Magnetically coupled microcalorimeters *J. Low Temp. Phys.* **167** 254–68
- [17] Verhoeve P, Martin D D E and Venn R 2010 Imaging soft x-ray spectrometers based on superconducting tunnel junctions *Proc. SPIE* **7742** 77420O
- [18] Angloher G, Huber M, Jochum J, Rüdiger A, von Feilitzsch F and Mößbauer R L 2002 Energy resolution $\Delta E = 12$ eV at 5.9 keV for lead absorber coupled to a single Al-stj via phonons *Low Temp. Detectors* **605** 23–6
- [19] Mazin B A, Bumble B, Day P K, Eckart M E, Golwala S, Zmuidzinas J and Harrison F A 2006 Position sensitive x-ray spectrophotometer using microwave kinetic inductance detectors *Appl. Phys. Lett.* **89** 222507
- [20] Cecil T, Gades L, Madden T, Yan D and Miceli A 2015 Optimization of thermal kinetic inductance detectors for x-ray spectroscopy *IEEE Trans. Appl. Supercond.* **1–1**
- [21] Nahum M and Martinis J M 1995 Hot-electron microcalorimeters as high-resolution x-ray detectors *Appl. Phys. Lett.* **66** 3203–5
- [22] Martin D D E, Verhoeve P, Peacock A, Kozorezov A G, Wigmore J K, Rogalla H and Venn R 2006 Resolution limitation due to phonon losses in superconducting tunnel junctions *Appl. Phys. Lett.* **88** 123510
- [23] Zehnder A 1995 Response of superconductive films to localized energy deposition *Phys. Rev. B* **52** 12858
- [24] Kozorezov A G, Volkov A F, Wigmore J K, Peacock A, Poelaert A and den Hartog R 2000 Quasiparticle-phonon downconversion in nonequilibrium superconductors *Phys. Rev. B* **61** 11807
- [25] Perinati E, Barbera M, Collura A, Serio S and Silver E 2004 Spectral broadening by incomplete thermalization of the energy in x-ray microcalorimeters with superconducting absorber and ntd-ge thermal sensor *Nucl. Instrum. Methods Phys. Res. A* **531** 459–66
- [26] Knoll G F 2010 *Radiation Detection and Measurement* (New York: Wiley)
- [27] Porter F S, Deiker S, Kelley R L, Lesser A, McCammon D, Stahle C K and Szymkowiak A E 1997 Energy loss due to photoelectron escape from HgTe absorbers in x-ray microcalorimeters *Proc. 7th Int. Workshop on Low Temperature Detectors*
- [28] Papp T 2003 On the response function of solid-state detectors, based on energetic electron transport processes *X-Ray Spectrom.* **32** 458–69
- [29] Ullom J N, Doriese W B, Fischer D A, Fowler J W, Hilton G C, Jaye C, Reintsema C D, Swetz D S and Schmidt D R 2014 Transition-edge sensor microcalorimeters for x-ray beamline science *Synchrotron Radiat. News* **27** 24–7
- [30] Kozorezov A G, Lambert C, Peterflavi C G, Bennett D, Hays-Wehle J, Horansky R D and Ullom J *Quasi-particle recombination in clean, anisotropic superconductors* in preparation
- [31] Cosulich E, Gatti F and Vitale S 1993 Further results on μ -calorimeters with superconducting absorber *J. Low Temp. Phys.* **93** 263–8
- [32] Chow D T, Lindeman M A, Cunningham M F, Frank M, Barbee T W Jr and Labov S E 2000 Gamma-ray spectrometers using a bulk Sn absorber coupled to a Mo/Cu multilayer superconducting transition edge sensor *Nucl. Instrum. Methods Phys. Res. A* **444** 196–200
- [33] Zink B L 2006 Array-compatible transition-edge sensor microcalorimeter γ -ray detector with 42 eV energy resolution at 103 keV *Appl. Phys. Lett.* **89** 124101–124101
- [34] Hatakeyama S, Ohno M, Takahashi H, Damayanthi R M T, Otani C, Yasumune T, Ohnishi T, Takasaki K and Koyama S 2014 Gamma-ray spectrometer based on a transition edge sensor for nuclear materials analysis *J. Low Temp. Phys.* **176** 560–5
- [35] Horansky Robert D, Bennett Douglas A, Schmidt Daniel R, Zink Barry L and Ullom Joel N 2013 Identification and elimination of anomalous thermal decay in gamma-ray microcalorimeters *Appl. Phys. Lett.* **103** 212602
- [36] Irimatsugawa T, Hatakeyama S, Ohno M, Takahashi H, Otani C and Maekawa T 2014 High energy gamma-ray spectroscopy using TES with a bulk tantalum absorber *IEEE Trans. Appl. Supercond.* **25** 2101303
- [37] Sellers G J, Anderson A C and Birnbaum H K 1974 Anomalous heat capacities of niobium and tantalum below 1 K *Phys. Rev. B* **10** 2771
- [38] Kotsubo V 2010 private communication
- [39] HR O'neal and Phillips N E 1965 Low-temperature heat capacities of indium and tin *Phys. Rev.* **137** A748

- [40] Bennett D A *et al* 2012 A high resolution gamma-ray spectrometer based on superconducting microcalorimeters *Rev. Sci. Instrum.* **83** 093113
- [41] Iyomoto N *et al* 2008 Close-packed arrays of transition-edge x-ray microcalorimeters with high spectral resolution at 5.9 keV *Appl. Phys. Lett.* **92** 013508
- [42] Kiviranta M, Seppa H, van den Kuur J and de Korte P 2002 Squid-based readout schemes for microcalorimeter arrays *AIP Conf. Proc.* (Bristol: Institute of Physics Publishing) pp 295–300
- [43] Chervenak J A, Irwin K D, Grossman E N, Martinis J M, Reintsema C D and Huber M E 1999 Superconducting multiplexer for arrays of transition edge sensors *Appl. Phys. Lett.* **74** 4043–5
- [44] Doriese W B *et al* 2007 14-pixel, multiplexed array of gamma-ray microcalorimeters with 47 eV energy resolution at 103 keV *Appl. Phys. Lett.* **90** 7
- [45] Drung D 2003 High-*tc* and low-*tc* dc squid electronics *Supercond. Sci. Technol.* **16** 1320
- [46] Bennett D A, Horansky R D, Hoover A S, Hoteling N J, Rabin M W, Schmidt D R, Swetz D S, Vale L R and Ullom J N 2010 An analytical model for pulse shape and electrothermal stability in two-body transition-edge sensor microcalorimeters *Appl. Phys. Lett.* **97** 102504
- [47] Holland W S, Duncan W D, Kelly B D, Irwin K D, Walton A J, Ade P A R and Robson E I 2003 SCUBA-2: a large format submillimetre camera on the James Clerk maxwell telescope *Proc. SPIE* **4855** 1–18
- [48] Smith S J *et al* 2015 Uniformity of kilo-pixel arrays of transition-edge sensors for x-ray astronomy *IEEE Trans. Appl. Supercond.* **25** 1–5
- [49] Porst J-P *et al* 2013 Time domain multiplexed readout of magnetically coupled calorimeters *IEEE Trans. Appl. Supercond.* **23** 2500905
- [50] Beyer J and Drung D 2008 A squid multiplexer with superconducting-to-normalconducting switches *Supercond. Sci. Technol.* **21** 105022
- [51] Niemack M D, Beyer J, Cho H M, Doriese W B, Hilton G C, Irwin K D, Reintsema C D, Schmidt D R, Ullom J N and Vale L R 2010 Code-division squid multiplexing *Appl. Phys. Lett.* **96** 163509
- [52] Beev N, Kiviranta M, van der Kuur J, Bruijn M, Brandel O, Linzen S, Fritzsche L, Ahoranta J, Penttilä J and Roschier L 2014 Cryogenic time-domain multiplexer based on squid arrays and superconducting/normal conducting switches *J. Phys.: Conf. Ser.* **507** 042003
- [53] Irwin K D, Niemack M D, Beyer J, Cho H M, Doriese W B, Hilton G C, Reintsema C D, Schmidt D R, Ullom J N and Vale L R 2010 Code-division multiplexing of superconducting transition-edge sensor arrays *Supercond. Sci. Technol.* **23** 034004
- [54] Irwin K, Cho H, Doriese W, Fowler J, Hilton G, Niemack M, Reintsema C, Schmidt D, Ullom J and Vale L 2012 Advanced code-division multiplexers for superconducting detector arrays *J. Low Temp. Phys.* **167** 1–7
- [55] Walsh J L 1923 A closed set of normal orthogonal functions *Am. J. Math.* **5**–24
- [56] Stiehl G M, Doriese W B, Fowler J W, Hilton G C, Irwin K D, Reintsema C D, Schmidt D R, Swetz D S, Ullom J N and Vale L R 2012 Code-division multiplexing for x-ray microcalorimeters *Appl. Phys. Lett.* **100** 072601
- [57] Karasik B and McGrath W 2001 Novel multiplexing technique for detector and mixer arrays *12th Int. Symp. on Space Terahertz Technology*
- [58] Fowler J W, Doriese W B, Hilton G, Irwin K, Schmidt D, Stiehl G, Swetz D, Ullom J N and Vale L 2012 Optimization and analysis of code-division multiplexed tes microcalorimeters *J. Low Temp. Phys.* **167** 713–20
- [59] Furukawa H and Shirae K 1989 Multichannel dc squid system *Japan. J. Appl. Phys.* **28** L456
- [60] Yoon J, Clarke J, Gildemeister J M, Lee A T, Myers M J, Richards P L and Skidmore J T 2001 Single superconducting quantum interference device multiplexer for arrays of low-temperature sensors *Appl. Phys. Lett.* **78** 371–3
- [61] Dobbs M A *et al* 2012 Frequency multiplexed superconducting quantum interference device readout of large bolometer arrays for cosmic microwave background measurements *Rev. Sci. Instrum.* **83** 073113
- [62] Dobbs M, Bissonnette E and Spieler H 2008 Digital frequency domain multiplexer for millimeter-wavelength telescopes *IEEE Trans. Nucl. Sci.* **55** 21–26
- [63] den Hartog R *et al* 2009 Baseband feedback for frequency-domain-multiplexed readout of tes x-ray detectors *13th Int. Workshop on Low Temperature Detectors—LTD13* vol 1185 (New York: AIP) pp 261–4
- [64] de Haan T, Smecher G and Dobbs M 2012 Improved performance of tes bolometers using digital feedback *Proc. SPIE* **8452** 84520E
- [65] MacDermid K *et al* 2014 The performance of the bolometer array and readout system during the 2012/2013 flight of the e and b experiment (ebex) *Proc. SPIE* **9153** 915311
- [66] Hattori K *et al* 2014 Optimization of cold resonant filters for frequency domain multiplexed readout of polarbear-2 *Proc. SPIE* **9153** 91531B
- [67] den Hartog R *et al* 2012 Low-noise readout of tes detectors with baseband feedback frequency domain multiplexing *J. Low Temp. Phys.* **167** 652–7
- [68] Cunningham M F, Ullom J N, Miyazaki T, Labov S E, Clarke J, Lanting T M, Lee A T, Richards P L, Yoon J and Spieler H 2002 High-resolution operation of frequency-multiplexed transition-edge photon sensors *Appl. Phys. Lett.* **81** 159–61
- [69] den Hartog R *et al* 2014 Requirements for the detectors and read-out of athena x-ifu *Proc. SPIE* **9144** 91445Q
- [70] Akamatsu H *et al* 2013 Single pixel characterization of x-ray tes microcalorimeter under ac bias at mhz frequencies *IEEE Trans. Appl. Supercond.* **23** 2100503–2100503
- [71] Akamatsu H *et al* 2014 Performance of tes x-ray microcalorimeters with ac bias read-out at mhz frequencies *J. Low Temp. Phys.* **1**–6
- [72] Gottardi L *et al* 2014 Josephson effects in an alternating current biased transition edge sensor *Appl. Phys. Lett.* **105** 162605
- [73] de Korte Piet AJ *et al* 2006 Eureka: a european-japanese micro-calorimeter array *Proc. SPIE* **6266** 62661Z
- [74] Day P K, LeDuc H G, Mazin B A, Vayonakis A and Zmuidzinas J 2003 A broadband superconducting detector suitable for use in large arrays *Nature* **425** 817–21
- [75] Zmuidzinas J 2012 Superconducting microresonators: physics and applications *Annu. Rev. Condens. Matter Phys.* **3** 169–214
- [76] Alpert B *et al* 2015 Holmes—the electron capture decay of ^{163}Ho to measure the electron neutrino mass with sub-eV sensitivity *Eur. Phys. J. C* **75** 3
- [77] Irwin K D and Lehnert K W 2004 Microwave squid multiplexer *Appl. Phys. Lett.* **85** 2107–9
- [78] Lehnert K W, Irwin K D, Castellanos-Beltran M A, Mates J A B and Vale L R 2007 Evaluation of a microwave squid multiplexer prototype *IEEE Trans. Appl. Supercond.* **17** 705–9
- [79] Hahn I, Day P, Bumble B and LeDuc H G 2008 Recent results of a new microwave squid multiplexer *J. Low Temp. Phys.* **151** 934–9
- [80] Mates J A B, Irwin K D, Vale L R, Hilton G C, Gao J and Lehnert K W 2012 Flux-ramp modulation for squid multiplexing *J. Low Temp. Phys.* **167** 707–12

- [81] Gao J, Zmuidzinas J, Mazin B A, LeDuc H G and Day P K 2007 Noise properties of superconducting coplanar waveguide microwave resonators *Appl. Phys. Lett.* **90** 102507
- [82] Mates J A B, Hilton G C, Irwin K D, Vale L R and Lehnert K W 2008 Demonstration of a multiplexer of dissipationless superconducting quantum interference devices *Appl. Phys. Lett.* **92** 023514
- [83] Mates J A B 2011 The microwave SQUID multiplexer *PhD Thesis* University of Colorado
- [84] Hirayama F, Kohjiro S, Fukuda D, Yamamori H, Nagasawa S and Hidaka M 2013 Microwave squid multiplexer for tes readout *IEEE Trans. Appl. Supercond.* **23** 2500405
- [85] Kohjiro S, Hirayama F, Yamamori H, Nagasawa S, Fukuda D and Hidaka M 2014 White noise of nb-based microwave superconducting quantum interference device multiplexers with nbn coplanar resonators for readout of transition edge sensors *J. Appl. Phys.* **115** 223902
- [86] Kempf S, Gastaldo L, Fleischmann A and Enss C 2014 Microwave squid multiplexer for the readout of metallic magnetic calorimeters *J. Low Temp. Phys.* **175** 850–60
- [87] Noroozian O *et al* 2013 High-resolution gamma-ray spectroscopy with a microwave-multiplexed transition-edge sensor array *Appl. Phys. Lett.* **103** 202602
- [88] Bennett D A, Mates J A B, Gard J D, Hoover A S, Rabin M W, Reintsema C D, Schmidt D R, Vale L R and Ullom J N 2014 Integration of tes microcalorimeters with microwave squid multiplexed readout *IEEE Trans. Appl. Supercond.* **25** 2101405
- [89] Gastaldo L *et al* 2014 The electron capture¹⁶³ho experiment echo *J. Low Temp. Phys.* **176** 876–84
- [90] Reintsema C D *et al* 2008 A tdma hybrid squid multiplexer *J. Low Temp. Phys.* **151** 927–33
- [91] Szymkowiak A E, Kelley R L, Moseley S H and Stahle C K 1993 Signal processing for microcalorimeters *J. Low Temp. Phys.* **93** 281–5
- [92] Doriese W B, Adams J S, Hilton G C, Irwin K D, Kilbourne C A, Schima F J and Ullom J N 2009 Optimal filtering, record length, and count rate in transition-edge-sensor microcalorimeters *13th Int. Workshop on Low Temperature detectors—LTD13* vol 1185 (New York: AIP) pp 450–3
- [93] Boyce K R *et al* 1999 Design and performance of the astro-el xrs signal processing system *Proc. SPIE* **3765** 741–50
- [94] Seta H *et al* 2012 The digital processing system for the soft x-ray spectrometer onboard astro-h—the design and the performance *IEEE Trans. Nucl. Sci.* **59** 366–72
- [95] Lee S J *et al* 2014 High count-rate studies of small-pitch transition-edge sensor x-ray microcalorimeters *J. Low Temp. Phys.* **1–7**
- [96] Tan H, Hennig W, Warburton W K, Doriese W B and Kilbourne C A 2011 Development of a real-time pulse processing algorithm for tes-based x-ray microcalorimeters *IEEE Trans. Appl. Supercond.* **21** 276–80
- [97] Alpert B K, Doriese W B, Fowler J W and Ullom J N 2012 Predicted energy resolution of a running-sum algorithm for microcalorimeters *J. Low Temp. Phys.* **167** 582–7
- [98] Tan H, Walby M, Hennig W, Warburton W K, Grudberg P, Reintsema C D, Bennett D A, Doriese W B and Ullom J N 2013 A digital signal processing module for time-division multiplexed microcalorimeter arrays *IEEE Trans. Appl. Supercond.* **23** 2500305
- [99] Alpert B K, Horansky R D, Bennett D A, Doriese W B, Fowler J W, Hoover A S, Rabin M W and Ullom J N 2013 Note: operation of gamma-ray microcalorimeters at elevated count rates using filters with constraints *Rev. Sci. Instrum.* **84** 056107
- [100] Fowler J *et al* 2015 *Astrophys. J. Suppl. Ser.* arXiv:1503.05989
- [101] Figueroa-Feliciano E, Cabrera B, Miller A J, Powell S F, Saab T and Walker A B C 2000 Optimal filter analysis of energy-dependent pulse shapes and its application to tes detectors *Nucl. Instrum. Methods Phys. Res. A* **444** 453–6
- [102] Fixsen D J, Moseley S H, Cabrera B and -Feliciano E F 2002 Optimal fitting of non-linear detector pulses with nonstationary noise *Low Temperature Detectors 9th Int. Workshop on Low Temperature Detectors* vol 605 (New York: AIP) pp 339–42
- [103] Whitford C H, Tiest W M B and Holland A D 2004 Practical considerations in optimal filtering of tes signals *Nucl. Instrum. Methods Phys. Res. A* **520** 592–4
- [104] Fixsen D J, Moseley S H, Gerrits T, Lita A E and Nam S W 2014 Optimal energy measurement in nonlinear systems: an application of differential geometry *J. Low Temp. Phys.* **1–11**
- [105] Busch S E 2013 private communication
- [106] Bandler S R, Figueroa-Feliciano E, Iyomoto N, Kelley R L, Kilbourne C A, Murphy K D, Porter F S, Saab T and Sadleir J 2006 Non-linear effects in transition edge sensors for x-ray detection *Nucl. Instrum. Methods Phys. Res. A* **559** 817–9
- [107] van der Kuur J and Kiviranta M 2013 Operation of transition edge sensors in a resistance locked loop *Appl. Phys. Lett.* **102** 023505
- [108] Shank B, Yen J J, Cabrera B, Kreikebaum J M, Moffatt R, Redl P, Young B A, Brink P L, Cherry M and Tomada A 2014 Nonlinear optimal filter technique for analyzing energy depositions in tes sensors driven into saturation *AIP Adv.* **4** 117106
- [109] Maasilta I J 2012 Complex impedance, responsivity and noise of transition-edge sensors: analytical solutions for two- and three-block thermal models *AIP Adv.* **2** 042110
- [110] Sadleir John E, Smith Stephen J, Bandler Simon R, Chervenak James A and Clem John R 2010 Longitudinal proximity effects in superconducting transition-edge sensors *Phys. Rev. Lett.* **104** 047003
- [111] Sadleir J E, Smith S J, Robinson I K, Finkbeiner F M, Chervenak J A, Bandler S R, Eckart M E and Kilbourne C A 2011 Proximity effects and nonequilibrium superconductivity in transition-edge sensors *Phys. Rev. B* **84** 184502
- [112] Likharev K K 1979 Superconducting weak links *Rev. Mod. Phys.* **51** 101
- [113] Kozorezov A *et al* 2011 Modeling the resistive state in a transition edge sensor *Appl. Phys. Lett.* **99** 063503
- [114] Coffey W T, Kalmykov Y P, Titov S V and Cleary L 2008 Smoluchowski equation approach for quantum brownian motion in a tilted periodic potential *Phys. Rev. E* **78** 031114
- [115] Kozorezov A G, Golubov A A, Martin D D E, de Korte P A J, Lindeman M A, Hijmering R A and Wigmore J K 2011 Microscopic model of a transition edge sensor as a weak link *IEEE Trans. Appl. Supercond.* **21** 250–3
- [116] Bennett D A, Swetz D S, Schmidt D R and Ullom J N 2013 Resistance in transition-edge sensors: a comparison of the resistively shunted junction and two-fluid models *Phys. Rev. B* **87** 020508
- [117] Ambegaokar V and Halperin B I 1969 Voltage due to thermal noise in dc josephson effect *Phys. Rev. Lett.* **22** 1364
- [118] Bennett D A, Swetz D S, Horansky R D, Schmidt D R and Ullom J N 2012 A two-fluid model for the transition shape in transition-edge sensors *J. Low Temp. Phys.* **167** 102–7
- [119] Smith S J *et al* 2013 Implications of weak-link behavior on the performance of mo/au bilayer transition-edge sensors *J. Appl. Phys.* **114** 074513

- [120] Jaklevic R C, Lambe J, Mercereau J E and Silver A H 1965 Macroscopic quantum interference in superconductors *Phys. Rev.* **140** 1628–37
- [121] Sadleir J E, Smith S J, Robinson I K, Finkbeiner F M, Chervenak J A, Bandler S R, Eckart M E and Kilbourne C A 2011 Proximity effects and nonequilibrium superconductivity in transition-edge sensors *Phys. Rev. B* **84** 184502
- [122] Barone A, Paterno G and Wiley J 1982 *Physics and Applications of the Josephson Effect* vol 1 (New York: Wiley)
- [123] Gottardi L *et al* 2014 Weak-link phenomena in ac-biased transition edge sensors *J. Low Temp. Phys.* **176** 279–84
- [124] Wang G, Yefremenko V, Chang C L, Novosad V, Mehl J, Pearson J, Divan R and Carlstrom J E 2013 Mo/au bilayer superconducting transition edge sensor tuning with surface modification structures *IEEE Trans. Appl. Supercond.* **23** 2101605
- [125] Beyer A D, Echtermach P M, Kenyon M E, Runyan M C, Bumble B, Bradford C M, Bock J J and Holmes W A 2013 Effect of mo/cu superconducting bilayer geometry on ultra-sensitive transition-edge sensor performance *IEEE Trans. Appl. Supercond.* **23** 2100104
- [126] Tinkham M 1996 *Introduction to Superconductivity* (New York: Dover)
- [127] Golubov A A, Yu Kupriyanov M and Il'ichev E 2004 The current–phase relation in Josephson junctions *Rev. Mod. Phys.* **76** 411
- [128] Zaikin A and Zharkov G 1981 Theory of wide dirty s-n junctions *Sov. J. Low Temp. Phys.* **7** 184
- [129] Kupriyanov M Y and Lukichev V F 1982 Influence of the proximity effect in the electrodes on the stationary properties of s-n-s josephson structures *Sov. J. Low Temp. Phys.* **8** (engl. transl.) (USA)
- [130] Poole C P, Farach H A, Creswick R J and Prozorov R 2010 *Superconductivity (Superconductivity Series)* (Amsterdam: Elsevier)
- [131] Irwin K D, Hilton G C, Wollman D A and Martinis J M 1998 Thermal-response time of superconducting transition-edge microcalorimeters *J. Appl. Phys.* **83** 3978
- [132] Skocpol W, Beasley M and Tinkham M 1974 Phase-slip centers and nonequilibrium processes in superconducting tin microbridges *J. Low Temp. Phys.* **16** 145
- [133] Pappas C G *et al* 2014 Optical efficiency and $r(t, i)$ measurements of actpol teses using time domain multiplexing electronics *J. Low Temp. Phys.* **1–6**
- [134] Taralli E, Lolli L, Portesi C, Monticone E, Rajteri M, Wang T, Chen J and Zhou X 2014 Reduced active area in transition-edge sensors for visible-nir photon detection: a comparison of experimental data and two-fluid model *IEEE Trans. Appl. Supercond.* **25** 2200304
- [135] Il'ichev E V, Kuznetsov V I and Tulin V A 1992 Conversion of phase-slip lines into elementary resistive domains in a current-carrying superconducting thin film *JETP Lett.* **56** 295–9
- [136] Dmitriev V M and Zolocheskii I V 2006 Resistive current states in wide superconducting films in zero magnetic field *Supercond. Sci. Technol.* **19** 342
- [137] Bezuglyi E V and Zolocheskii I V 2010 Phase diagram of a current-carrying superconducting film in the absence of a magnetic field *Low Temp. Phys.* **36** 1008
- [138] Dmitrenko I M 1996 Resistive state of broad superconducting films and phase-slip lines (a review) *Low Temp. Phys.* **22** 648
- [139] Schmid A and Schön G 1975 Linearized kinetic equations and relaxation processes of a superconductor near t_c *J. Low Temp. Phys.* **20** 207–27
- [140] Kadin A M, Skocpol W J and Tinkham M 1978 Magnetic field dependence of relaxation times in nonequilibrium superconductors *J. Low Temp. Phys.* **33** 481–503
- [141] Tinkham M 1979 The interaction of phase-slip centers in superconducting filaments *J. Low Temp. Phys.* **35** 147–51
- [142] Bennett D A, Schmidt D R, Swetz D S and Ullom J N 2014 Phase-slip lines as a resistance mechanism in transition-edge sensors *Appl. Phys. Lett.* **104** 042602
- [143] Berdiyrov G R, Elmurodov A K, Peeters F M and Vodolazov D Y 2009 Finite-size effect on the resistive state in a mesoscopic type-ii superconducting stripe *Phys. Rev. B* **79** 174506
- [144] Kotsubo V, Bennett D A, Croce M P, Rabin M W, Schmidt D R and Ullom J N 2013 Observation of bias-specific telegraph noise in large transition-edge sensors *IEEE Trans. Appl. Supercond.* **23** 2100203
- [145] Kozorezov A G, Golubov A A, Martin D D E, de Korte P A J, Lindeman M A, Hijmering R A and Wigmore J K 2011 Microscopic model of a transition edge sensor as a weak link *IEEE Trans. Appl. Supercond.* **21** 250–3
- [146] Lindeman M, Khosropanah P, Hijmering R, Ridder M, Gottardi L, Bruijn M, vander Kuur J, de Korte P, Gao J and Hoevers H 2012 Complex impedance and equivalent bolometer analysis of a low noise bolometer for safari *J. Low Temp. Phys.* **167** 96–101
- [147] Smith S J *et al* 2013 Characterization of mo/au transition-edge sensors with different geometric configurations *J. Low Temp. Phys.* **176** 356–62
- [148] Taralli E, Portesi C, Lolli L, Rajteri M, Monticone E, Novikov I and Beyer J 2012 Impedance measurements for photon number resolving transition-edge sensors *Eur. Phys. J. Plus* **127** 1–7
- [149] Palosaari M R J, Kinnunen K M, Ridder M L, van der Kuur J, Hoevers H F C and Maasilta I J 2012 Analysis of impedance and noise data of an x-ray transition-edge sensor using complex thermal models *J. Low Temp. Phys.* **167** 129–34
- [150] Becker D T 2014 Submillimeter video imaging with a superconducting bolometer array *PhD Thesis* The University of Colorado, Boulder
- [151] Wang T-S, Guo G-C, Zhu Q-F, Wang J-X, Li T-F, Liu J-S, Chen W and Zhou X 2012 Device modeling of superconductor transition-edge sensors based on the two-fluid theory *IEEE Trans. Appl. Supercond.* **22** 2100212
- [152] Chow D T, Loshak A, van den Berg M L, Frank M A, Barbee T W Jr and Labov S E 2000 High-resolution gamma-ray spectrometers using bulk absorbers coupled to mo/cu multilayer superconducting transition-edge sensors *Int. Soc. Opt. Photonics* **4141** 67–75
- [153] Bacrania M K *et al* 2009 Large-area microcalorimeter detectors for ultra-high-resolution x-ray and gamma-ray spectroscopy *IEEE Trans. Nucl. Sci.* **56** 2299–302
- [154] Hoover A S *et al* 2009 Microcalorimeter arrays for ultra-high energy resolution x-and gamma-ray detection *J. Radioanal. Nucl. Chem.* **282** 227–32
- [155] Pibida L 2012 Measurements for the development of a simulated naturally occurring radioactive material *J. Res. Natl. Inst. Stand. Technol.* **117** 154–67
- [156] Kouzes R, Ely J, Evans J, Hensley W, Lepel E, McDonald J, Schweppe J, Siciliano E, Strom D and Woodring M 2006 Naturally occurring radioactive materials in cargo at US borders *Packag. Transp. Storage Secur. Radioact. Mater.* **17** 11–17
- [157] Friedrich S 2007 Nuclear diagnostics with cryogenic spectrometers *Nucl. Instrum. Methods Phys. Res. A* **579** 157–60
- [158] Jethava N 2009 Improved isotopic analysis with a large array of gamma-ray microcalorimeters *IEEE Trans. Appl. Supercond.* **19** 536–9

- [159] Winkler R *et al* 2015 256-Pixel microcalorimeter array for high-resolution γ -ray spectroscopy of mixed-actinide materials *Nucl. Instrum. Methods Phys. Res. A* **770** 203–10
- [160] Sampson T E, Nelson G W and Kelley T A 1989 Fram: a versatile code for analyzing the isotopic composition of plutonium from gamma-ray pulse height spectra *Technical Report Los Alamos National Lab., NM (USA)*LA-11720-MS
- [161] Hoover A S *et al* 2013 Determination of plutonium isotopic content by microcalorimeter gamma-ray spectroscopy *IEEE Trans. Nucl. Sci.* **60** 681–8
- [162] Hoover A S *et al* 2014 Uncertainty of plutonium isotopic measurements with microcalorimeter and high-purity germanium detectors *IEEE Trans. Nucl. Sci.* **61** 2365–72
- [163] Stahle C K 1992 The development of high-resolution calorimetric x-ray detectors for Compton scattering experiments *PhD Thesis* Stanford University
- [164] Silver C S, Beeman J, Piccirillo L, Timbie P T and Zhou J W 2002 Optimization of a 6lif bolometric neutron detector *Nucl. Instrum. Methods Phys. Res. A* **485** 615–23
- [165] Horansky R D *et al* 2008 Superconducting calorimetric alpha particle sensors for nuclear nonproliferation applications *Appl. Phys. Lett.* **93** 22
- [166] Loidl M, Rodrigues M, Censier B, Kowalski S, Mougeot X, Cassette P, Branger T and Lacour D 2010 First measurement of the beta spectrum of 241 pu with a cryogen detector *Appl. Radiat. Isot.* **68** 1454–8
- [167] Lee S-J, Lee M K, Jang Y S, Kim I H, Kim S K, Lee J S, Lee K B, Lee Y H and Kim Y-H 2010 Cryogenic measurement of alpha decay in a 4π absorber *J. Phys. G: Nucl. Part. Phys.* **37** 055103
- [168] Hoover A S *et al* 2015 Measurement of the 240pu/239pu mass ratio using a transition-edge-sensor microcalorimeter for total decay energy spectroscopy *Anal. Chem.* **87** 3996–4000
- [169] Ardito R *et al* 2006 The cuoricino and cuore double beta decay experiments *Prog. Part. Nucl. Phys.* **57** 203–16
- [170] Engle J W, Birnbaum E R, Trelue H R, John K D, Rabin M W and Nortier F M 2013 Evaluation of 163 ho production options for neutrino mass measurements with microcalorimeter detectors *Nucl. Instrum. Methods Phys. Res. A* **311** 131–8
- [171] Wollman D A, Irwin K D, Hilton G C, Dulcie L L, Newbury D E and Martinis J M 1997 High-resolution, energy-dispersive microcalorimeter spectrometer for x-ray microanalysis *J. Microsc.* **188** 196–223
- [172] Isaila C, Feilitzsch F, Hühne J, Hollerith C, Phelan K, Simmnacher B, Weiland R and Wernicke D 2006 X-ray microanalysis with microcalorimeters *Nucl. Instrum. Methods Phys. Res. A* **559** 734–6
- [173] Jach T, Ritchie N, Ullom J and Beall J A 2007 Quantitative analysis with the transition edge sensor microcalorimeter x-ray detector *Powder Diffr.* **22** 138–41
- [174] Krause M O and Oliver J H 1979 Natural widths of atomic k and l levels, ka x-ray lines and several kll auger lines *J. Phys. Chem. Ref. Data* **8** 329–38
- [175] Fischer D W and Baun W L 1965 Effect of chemical combination on the soft x-ray k emission bands of nitrogen and carbon *J. Chem. Phys.* **43** 2075–8
- [176] Nordfors B 1955 A note on the α ka_3 α_4 lines in metal and oxide *Proc. Phys. Soc. A* **68** 654
- [177] Wollman D A, Nam S W, Newbury Dale E, Hilton G C, Irwin K D, Bergren N F, Deiker S, Rudman D A and Martinis J M 2000 Superconducting transition-edge-microcalorimeter x-ray spectrometer with 2 eV energy resolution at 1.5 keV *Nucl. Instrum. Methods Phys. Res. A* **444** 145–50
- [178] Wollman D A, Newbury Dale E, Hilton G C, Irwin K D, Dulcie L L, Bergren N F and Martinis J M 1998 Microcalorimeter eds measurements of chemical shifts in Fe compounds *Microsc. Microanal.* **4** 196–7
- [179] Nam S W, Wollman D A, Newbury D E, Hilton G C, Irwin K D, Rudman D A, Deiker S, Bergren N F and Martinis J M 2001 Progress towards arrays of microcalorimeter x-ray detectors *Microsc. Microanal.* **7** 1050–1
- [180] Redfern D, Joe N, Hohne J, Weiland R, Simmnacher B and Hollerich C 2002 The microcalorimeter for industrial applications *J. Res. Natl. Inst. Stand. Technol.* **107** 621–6
- [181] Cantor R and Naito H 2012 Practical x-ray spectrometry with second-generation microcalorimeter detectors *Microsc. Today* **20** 38–42
- [182] Terborg R, Cantor R and Naito H 2012 Characterization of a microcalorimeter in comparison to silicon drift detectors *Microsc. Microanal.* **18** 1060–1
- [183] Geer R E, Wu D and Wollman D A 2002 High-resolution energy-dispersive x-ray spectroscopic analysis of ultrathin ion diffusion barriers using microcalorimetry *J. Appl. Phys.* **91** 1099–103
- [184] Lordi V, Gambin V, Friedrich S, Funk T, Takizawa T, Uno K and Harris J S 2003 Nearest-neighbor configuration in (gain)(nas) probed by x-ray absorption spectroscopy *Phys. Rev. Lett.* **90** 145505
- [185] Shiki S, Ukibe M, Kitajima Y and Ohkubo M 2012 X-ray detection performance of 100-pixel superconducting tunnel junction array detector in the soft x-ray region *J. Low Temp. Phys.* **167** 748–53
- [186] Doriese R 2015 private communication
- [187] Uhlig J *et al* 2015 High-resolution x-ray emission spectroscopy with transition-edge sensors, present performance and future potential *J. Synchrotron Radiat.* doi:10.1107/S1600577515004312
- [188] Moseley S H, Mather J C and McCammon D 1984 Thermal detectors as x-ray spectrometers *J. Appl. Phys.* **56** 1257–62
- [189] Ness J-U, Mewe R, Schmitt J H M M, Raassen A J J, Porquet D, Kaastra J S, van der Meer R L J, Burwitz V and Predehl P 2001 Helium-like triplet density diagnostics *Astron. Astrophys.* **367** 282–96
- [190] McCammon D *et al* 2008 The x-ray quantum calorimeter sounding rocket experiment: improvements for the next flight *J. Low Temp. Phys.* **151** 715–20
- [191] Kelley R L *et al* 2007 The Suzaku high resolution x-ray spectrometer *Publ. Astron. Soc. Japan* **59** 77–112
- [192] Mitsuda K *et al* 2010 The high-resolution x-ray microcalorimeter spectrometer system for the SXS on Astro-H *Proc. SPIE* **7732** 773211
- [193] F-Feliciano E *et al* 2012 Update on the micro-x sounding rocket payload *Proc. SPIE* **8443** 84431B
- [194] Silver E *et al* 2000 Laboratory astrophysics survey of key x-ray diagnostic lines using a microcalorimeter on an electron beam ion trap *Astrophys. J.* **541** 495
- [195] Porter F S, Brown G V, Boyce K R, Kelley R L, Kilbourne C A, Beiersdorfer P, Chen H, Terracol S, Kahn S M and Szymkowiak A E 2004 The astro-e2 x-ray spectrometer/ebit microcalorimeter x-ray spectrometer *Rev. Sci. Instrum.* **75** 3772–4
- [196] Beiersdorfer P *et al* 2003 Laboratory simulation of charge exchange-produced x-ray emission from comets *Science* **300** 1558–9
- [197] Gabriele L *et al* 2014 The transition-edge ebit microcalorimeter spectrometer *Proc. SPIE* **9144** 91443U
- [198] Reis M A, Chaves P C and Taborda A 2011 Radiative Auger emission satellites observed by microcalorimeter-based energy-dispersive high-resolution PIXE *X-Ray Spectrom.* **40** 141–6

- [199] Palosaari M R J *et al* 2013 Transition-edge sensors for particle induced x-ray emission measurements *J. Low Temp. Phys.* **176** 285–90
- [200] Zamponi F, Ansari Z, Korff Schmising C v, Rothhardt P, Zhavoronkov N, Woerner M, Elsaesser T, Bargheer M, Troitzsch-Ryll T and Haschke M 2009 Femtosecond hard x-ray plasma sources with a kilohertz repetition rate *Appl. Phys. A* **96** 51–58
- [201] Uhlig J *et al* 2013 Table-top ultrafast x-ray microcalorimeter spectrometry for molecular structure *Phys. Rev. Lett.* **110** 138302
- [202] Okada S *et al* 2014 High-resolution kaonic-atom x-ray spectroscopy with transition-edge-sensor microcalorimeters *J. Low Temp. Phys.* 1–7
- [203] Deslattes R D, Jr E G K, Indelicato P, de Billy L, Lindroth E and Anton J 2003 X-ray transition energies: new approach to a comprehensive evaluation *Rev. Mod. Phys.* **75** 35
- [204] Wang C, Thummes G and Heiden C 1997 A two-stage pulse tube cooler operating below 4 k *Cryogenics* **37** 159–64
- [205] Hagmann C and Richards P L 1994 Two-stage magnetic refrigerator for astronomical applications with reservoir temperatures above 4 k *Cryogenics* **34** 221–6
- [206] Miller N A, Ullom J N, Beall J A, Hilton G C, Deiker S, Doriese W B, Irwin K D, Reintsema C D, Vale L R and Xu Y 2004 Robust infrared filters for x-ray spectroscopy *Nucl. Instrum. Methods Phys. Res. A* **520** 638–40
- [207] Grove D A, Betcher J C, Lairson B, Smith R and Ayers T 2010 Blocking filters with enhanced throughput for x-ray microcalorimetry *Proc. SPIE* **7739** 773940